DEUTSCHES ELEKTRONEN-SYNCHROTRON **DESY**

DESY 78/26
May 1978

ELASTIC AND INELASTIC ϕ-PHOTOPRODUCTION

by

H.-J. Behrend, J. Bodenkamp, W. P. Hesse,
W. A. McNeely Jr. and T. Miyachi

Deutsches Elektronen-Synchrotron DESY, Hamburg

D. C. Fries, P. Heine, H. Hirschmann, A. Markou and E. Seitz

Institut für Kernphysik des Kernforschungszentrum
and
Institut für Experimentelle Kernphysik der Universität Karlsruhe

NOTKESTRASSE 85 · 2 HAMBURG 52

To be sure that your preprints are promptly included in the
HIGH ENERGY PHYSICS INDEX ,
send them to the following address (if possible by air mail) :

DESY
Bibliothek
Notkestrasse 85
2 Hamburg 52
Germany

DESY 78/26
May 1978

E R R A T A

Page 2: Equation (1.2.) $\gamma p \to \phi X \to K^+K^- X \; (X \neq p)$

Page 3: Equation (2.1.) $f_\gamma(\gamma B \to VB) = \sum_{V'} \sqrt{\frac{\alpha}{4}\frac{4\pi}{\gamma_V^2}}\, f_V(V'B \to VB)$

Equation (2.2.) $f_\gamma(\gamma + p \to \phi p) = \sqrt{\frac{\alpha}{4}\frac{4\pi}{\gamma_\phi^2}}\, f_\phi(\phi' + p \to \phi + p)$

Page 16: The correct value of $\alpha'(0)$ stated in the last line is 0.19 ± 0.02 GeV $^{-2}$.

Elastic and Inelastic ϕ-Photoproduction

H.-J. Behrend, J. Bodenkamp, W. P. Hesse [+)], W. A. McNeely Jr. [++)] and T. Miyachi [+++)]

Deutsches Elektronen-Synchrotron, DESY, Hamburg

D. C. Fries, P. Heine [++++)], H. Hirschmann [+++++)], A. Markou and E. Seitz

Institut für Kernphysik des Kernforschungszentrum und Institut für Experimentelle Kernphysik der Universität Karlsruhe

[+)] Now: Department of Physics, Randolph-Macon College, Ashland, Va. 23005, U.S.A.

[++)] Now: Boeing Computer Services, Seattle, Washington 91868, U.S.A.

[+++)] Now: Institute for Nuclear Study, University of Tokyo, Tanashi, Tokyo 188, Japan

[++++)] Now: II. Institut für Experimental Physik der Universität Hamburg, Luruper Chaussee 149, D-2000 Hamburg 52

[+++++)] Now: SIN, Swiss Institute for Nuclear Research, CH-5234 Villingen

Abstract

The differential cross section of the reaction ($\gamma p \to p\phi$) has been measured in the t range $0 \leq t \leq 0.4$ GeV^2 and for photon energies from 3.0 to 6.7 GeV. In particular for the small t region the measurement accuracy was better than 10 %.

We obtained for the slope parameter B in an exponential parametrization of the differential cross section $\frac{d\sigma}{dt} = A\, e^{-B\,t}$ values of $B \approx 6 \pm 0.5$ GeV^{-2} which are significantly larger than the slopes obtained by most other experiments at higher t values. This indicates a t dependence of B particulary in the small t regior.

An energy dependence of the optical point $\left.\frac{d\sigma}{dt}\right|_{t=0}$, observed in our measurements, has been explained as a kinematic effect due to the VDM relation. A fit of our measurements is in excellent agreement with all other published values of $\left.\frac{d\sigma}{dt}\right|_{t=0}(\gamma p \to \phi p)$, this implies that $\sigma_{tot}(\phi p)$ must be essentially energy independent in this energy range.

Spin density matrix elements of the ϕ have been evaluated and an analysis of the helicity amplitudes has been carried out. This analysis confirmed s-channel helicity conservation.

Moments of spherical harmonics of the $K\bar{K}$ angular decay distribution have been computed for 10 MeV $K\bar{K}$ mass-bins from threshold to 1.3 GeV.

The mass dependence of the normalized moments is generally smooth. Contributing amplitudes have essentially only even moments. The moment $\langle Y_2^0 \rangle / \langle Y_0^0 \rangle$ changes sign above the ϕ mass.

Differential cross sections for the inelastic ϕ production $\gamma p \to \phi X$ have been evaluated for the first time both with respect to $t-t_{min}$ and M_X. The integrated inelastic cross sections are comparable in size with the elastic ones. The slopes of the differential cross sections $d\sigma/dt$ appear to become flater with increasing M_X.

§1. INTRODUCTION

In this paper [1] results are presented which were obtained from the measurement and analysis of photoproduced K^+K^- final states with an invariant mass near the phi meson mass (1020 MeV).

The data have been taken in a high statistics experiment performed at DESY using a tagged-photon beam, a forward wire-chamber magnetic spectrometer and a threshold Cerenkov counter. The analysis was essentially concerned with two reaction channels

$$\gamma p \rightarrow \phi p \rightarrow K^+K^-p \quad , \tag{1.1}$$

which will be called the 'elastic ϕ-photoproduction' (in the spirit of the vector-meson dominance picture), and

$$\gamma p \rightarrow \phi p \rightarrow K^+K^-X \quad (X \neq p) \quad , \tag{1.2}$$

which will be referred to as 'inelastic ϕ photoproduction'.

Reaction (1.1) has been studied for photon energies E_γ in the range from 3.0 to 6.7 GeV, reaction (1.2) in the energy range $4.6 \leq E_\gamma \leq 6.7$ GeV. In reaction (1.2) the missing mass lies in the interval $1.20 \leq M_X \leq 2.1$ GeV.

Phi photoproduction has been measured previously in a number of experiments up to photon energies of about 20 GeV [2], using mostly a Bremsstrahlung photon beam. This experiment has several distinguishing features in comparison with other phi-meson photoproduction experiments:

- It is the first high statistics experiment to systematically analyse the small t-region, $|t| < 0.4$ GeV^2.
- The measurement of the incident photon energy and the possibility to reconstruct the kinematic of an elastic event assured the separation of elastic and inelastic events.

§2. Theoretical Interest in ϕ Photoproduction

The interest in the photoproduction of the ϕ meson is closely connected to two rather fundamental theoretical problems in particle physics: the photon-hadron coupling and the diffractive scattering of hadrons.

Firstly, the phi is a neutral isoscalar meson resonance at a mass of 1020 MeV with spin, parity and charge conjugation identical to the photon, namely, $J^{PC} = 1^{--}$. Due to the similarity of the ϕ and γ quantum numbers, the ϕ (as well as the other vector mesons) plays an important role in photon physics for photon energies greater than a few GeV.

The vector-meson dominance model (VDM) describes an equivalence between the amplitude f_γ of the photon induced reaction $\gamma + B \to V + B$, and that caused by a transversely polarized vector meson ($V' + B \to V + B$), namely,

$$f_\gamma(\gamma B \to VB) = \sum_{V'} \sqrt{\frac{\alpha}{4} \frac{4\pi}{\gamma_V^2}} f_V(V'B \to VB) \quad , \tag{2.1}$$

where α is the fine-structure constant, $\gamma_V^2/4\pi$ is the γ-V coupling constant and V' represents the transverse part of the vector mesons ρ, ω, ϕ (because of the energy domain discussed, contributions of the ψ family can be neglected) and B the target nucleon. So that for the case of ϕ photoproduction on protons the amplitude from eq. (2.1) is of the following form:

$$f_\gamma(\gamma + p \to \phi + p) = \sqrt{\frac{\alpha}{4} \frac{4\pi}{\gamma_\phi^2}} f_\phi(\phi' + p \to \phi + p) \quad , \tag{2.2}$$

where contributions from mixed terms (e.g. $\rho p \to \phi p$) are assumed to be negligible. Hence the ϕ photoproduction is related to the hadronic reaction, $\phi' + p \to \phi + p$ (Fig. 1).

The second point of interest is the SU(3) assignment of the ϕ meson [3]. With the assumption of an ideal singlett-octett-mixing the ϕ is build solely from s and $\bar{s}$ quarks. This assumption is experimentally supported for example by the measurement of the ratio $\sigma(\pi^- p \to \phi n)/\sigma(\pi^- p \to \omega n) = 0.035 \pm 0.0010$, [4] which is equal to the fraction of non-strange quarks contained in the phi.

The Okubo-Zweig-Iizuka-rule then predicts that a direct interaction of the ϕ with particle states build only from non-strange quarks is strongly inhibited [4].

Because there are no strange direct s- and u-channel resonances which could couple to the ϕ, only the t-channel exchanges with CP = ++ and I=0 (as required by charge conjugation invariance) can contribute, that is only trajectories such as the pomeron, f (1270) and f' (1514).

However due to its non-strange quark content, the P' trajectory, which is identified with the f (1270), decouples in the t-channel [*]. Even if one assumes a similar nature for f' (1514) as for the ϕ meson, the exchange of the associated trajectory (P") would be suppressed by its low lying nature [**]. Thus the elastic ϕp-scattering is considered to occur through the exchange of only the pomeron trajectory.

From eq. (2.2), one obtains the differential cross sections for the photoproduction:

$$\frac{d\sigma}{dt}(\gamma p \to \phi p) = \frac{\alpha}{4} \frac{4\pi}{\gamma_\phi^2} \left(\frac{p_\phi}{k}\right)^2 \frac{d\sigma}{dt}(\phi p \to \phi p) \,, \tag{2.3}$$

where p_ϕ is the momentum of the ϕ meson, k is that of the incident photon in the center of mass system and t is the four momentum transfer squared. The total cross section of the reaction $\sigma_T(\phi p \to \phi p)$ is obtained by the optical theorem:

$$\left(\frac{d\sigma(\gamma p \to \phi p)}{dt}\right)_{t=0} = \frac{\alpha}{64\pi} \frac{4\pi}{\gamma_\phi^2} (1+\eta_\phi)^2 \left(\frac{p_\phi}{k}\right)^2 \sigma_T^2(\phi p \to \phi p), \tag{2.4}$$

where $(d\sigma/dt)_{t=0}$ is the extrapolated optical point and η_ϕ is the ratio of real to imaginary amplitudes at t=0.

In particular the energy dependence of the differential cross section and of the slope parameter can be analyzed applying the Regge model and a simple pole picture for the Pomeron trajectory. Although the naive pole picture for the Pomeron trajectory is generally untenable, as diffraction scattering data at very high energy have demonstrated, it may, at our energy range, still be a useful parametrization. Thus we parametrize the cross section in terms of a single pole exchange

$$\frac{d\sigma}{dt} = F(t) \left(\frac{s}{s_o}\right)^{2(\alpha(t)-1)} , \tag{2.5}$$

where s is the center of mass energy squared, s_o is a scale factor customarily set to 1 GeV^2, $\alpha(t)$ is the exchanged trajectory and F(t) represents the square of the residue function. For the pomeron trajectory $\alpha(t)$ is parametrized as $\alpha_p(t) = 1 + \alpha_p'(0)t$ with the slope parameter $\alpha_p'(0)$. The residue function is assumed to be

$$F(t) = A \exp(at + bt^2) , \tag{2.6}$$

where A, a and b are parameters determined by experimental data.

Consequently the differential cross section is described as follow:

$$\frac{d\sigma}{dt} = A \cdot \exp(m(s,t)) , \tag{2.7}$$

with

$$m(s,t) = (a + 2\alpha'(0) \cdot \ln(s/s_0)) \cdot t + bt^2 . \tag{2.8}$$

An additional insight into the diffractive nature of the ϕ photoproduction can be obtained studying the ϕ decay.

The analysis of the decay angular distribution of the $K\bar{K}$ system provides information on the dynamics of the reaction (1.1) by establishing the statistical population of the spin states of the ϕ, with their mass- and their t-dependence. It has been proposed that the s channel helicity conservation is an essential feature of a diffractive process [7]. Thus studying the helicity structure of the ϕ production gives some information on the dynamics of pomeron exchange. Pomeron exchange is a model of diffraction scattering on one hand and at the same time a feature of ϕ photoproduction suggested by the Quark model.

§3. Experimental Procedures

3a Experimental Set Up

A schematic drawing of the experimental set up is presented in Fig. 2. An electron beam was ejected from the synchrotron with a momentum spread $\Delta p/p = 0.25$ %. The beam was horizontally focussed to a 1 x 10 mm^2 shape on an aluminium radiator of 1 mm thickness. Downstream of the radiator, a tagging system was placed to analyse the momentum of the deflected electrons. The non-interacting electron beam was absorbed in a quantameter used for overall flux normalization.

While traversing an evacuated beam pipe to a liquid hydrogen target, the photon beam passed through a 20 cm long lead collimator, a pair of beam scrapers each remotely controlled in vertical and horizontal directions, a sweeping magnet and a lead-concrete wall.

At the liquid hydrogen target (50 cm long and 2.5 cm diameter), the photon beam was nearly Gaussian shaped with a half width of 7 mm. The target was surrounded by a hodoscope which consisted of 23 scintillation counters each 3.3 x 57.5 cm^2 extended parallel to the beam in a cylindrical array of 26 cm diameter. This hodoscope was inside the vacuum tank of the hydrogen target. The light was directed through optical guides to the outside. The target hodoscope detected the recoil protons and measured their azimuthal angles, thus checking the coplanarity condition between recoil proton and reconstructed kaon pair system.

Photons, which did not interact in the target, as well as electrons produced in materials along the beam line, passed through a hole in the front trigger counters, traversed four planes of multiwire proportional chambers and hit a 60 cm long lead absorber suspended at the entrance of a large aperture analysing magnet.

Hadrons produced at larger angles passed through (1) an array of front trigger counters, (2) four multiwire proportional chambers, (3) the large aperture analysing magnet with a field strength of 9.5 kG-meter, (4) a set of eight spark chambers each 1 x 1 m^2 with magnetic core readout, (5) a double wall of trigger counters and (6) a gas threshold Cerenkov

counter which discriminated against electrons and pions. The specifications of each component are presented in Table 1 a.

Data have been taken in three periods, each with a different incident electron energy as shown in Table 2. For the lower energy runs (Exp. II and III) a different experimental configuration from the one explained above was used to compensate for a reduction of detection efficiency of the spectrometer. The configuration was modified as follows:

- an array of 16 scintillation counters extending vertically replaced the front trigger counters mentioned above;
- only the larger multiwire proportional chambers with vertical and horizontal readout were used;
- an additional array of 12 trigger counters was placed between the analysing magnet and the first spark chamber (M-hodoscope);
- the target and the beam stopper were moved deeper inside the spectrometer magnet;
- the recoil proton hodoscope was removed.

Details are also tabulated in Table 1 b.

3b Tagging system

The photon beam was generated by the bremsstrahlung of the electrons traversing the radiator. Their recoil electrons were deflected and passed through an array of three layers of scintillation counters which tagged the bremsstrahlung photons impinging on the hydrogen target.

The first layer consisted of a picket-fence array of 22 scintillation counters each overlapping 1/3 of its neighbour. This counter array separated the recoil momentum into 43 bins each with a width of 48.1 Mev. Thus the tagging system covered an energy band of photons over 2.02 GeV with a top energy of $E_{top} = E-0.5$ GeV, where E is the energy of the incident electron beam.

The second and third layers consisted of 14 scintillation counters in pairs behind the first layer. They were used in two-fold coincidence in the trigger to give precise timing information and to monitor the flux of incident photons.

Calibration runs were made to investigate basic properties of the system: the energy calibration, the intensity dependence of the rate of multiple tags and the tagging efficiency.

For the energy calibration, electron pairs produced in a thin target in front of the magnet by tagged photons were observed. By reconstructing the electron pair tracks, the energy of the pair was calculated and compared with the photon energy from the tagging system. Although the resolution of the pair spectrometer does not match the resolution of the tagging counters (± 25 Mev), the center energy of each counter could be determined rather precisely to about ± 10 Mev. This was also checked against the position of the recoil mass of an elastically produced ϕ meson.

The tagging efficiency, defined as the ratio of the number of photons arriving at the target position to that of electrons triggering the tagging system, was measured by placing a shower counter at the target position. The efficiency was 89 ± 2 %.

At typical running conditions a beam of 2×10^5 tagged quanta per second (10 % duty cycle) was used. The rate of multiple tags was 12 % without accidental ones. Only single tags were accepted in the experiment. The measured cross section is based on the number of recorded single tags corrected for tagging efficiency.

Fig. 3 shows an observed bremsstrahlung spectrum in the tagging window.

3c The Cerenkov Counter

The counter consisted of a cylindrical steel tank with 2.40 m diameter and 2.33 m width positioned in the beam line behind the trigger counters with horizontal axis. Particles traversing the 2.1 x 1.0 m^2 steel entrance window of 3 mm thickness travelled through a radiator of about 1.7 m length. The light was focused by 6 spherical mirrors of 70 x 70 cm^2 each with an aluminium light collector into the photocathodes of six 58-UVP phototubes through quartz windows. With Freon-13 at 4 bar the maximum Cerenkov angle (particles of the light speed) was 70 mrad. For these particles an angular divergence of ± 50 mrad could be accepted, which agrees with the divergence of the particle stream hitting the counter for momenta higher than 1.6 GeV (threshold for pions). The counter is shown on Fig. 4.

The phototubes were run at 2.5 KV yielding pulses of about 1 volt for high energy electrons. The efficiency of the counter was measured by triggering the apparatus on two charged particles in front of and behind the magnet. By using the copiously produced ρ^os, π mesons with momenta between 2 and 4 GeV were identified and the π meson signals in the Cerenkov counter were recorded. The test gave an average detection efficiency of 98 ± 2 %. Since the counter was used in veto-mode, no effort was made to gain a more accurate number.

3d Data Taking

An event was recorded when the following trigger requirement TR was fulfilled:

$$TR = T(\geq 1) \cdot F(\geq 2) \cdot B(\geq 2) \cdot \bar{C} \quad \text{in Exp I,}$$

$$TR = T(\geq 1) \cdot F(\geq 2) \cdot M(\geq 2) \cdot B(\geq 2) \cdot \bar{C} \quad \text{in Exp II and III,}$$

where

$T(\geq 1)$ is an OR-signal formed from a two-fold coincidence between any two overlapping back-up counters of the tagging system;

$T(>2)$ is the majority coincidence that at least two of the front trigger counters have fired;

$M(\geq 2)$ is the majority coincidence that at least two counters of the M-hodoscope have fired;

$B(\geq 2)$ is the majority coincidence that at least two two-fold coincidences of overlapping counters occured in the trigger counters behind the spark chambers;

$\bar{C}$ is the absence of a signal from any of the six photomultipliers of the Cerenkov counters.

The spark chamber and proportional chamber addresses determining the particle traces, latches representing the status of all scintillation counters, the ADC's monitoring the pulse heights of the recoil hodoscope and of the Cerenkov counter photomultipliers were read via a CAMAC system into an on-line PDP-8/E computer, which furnished event and histogram displays and buffered the data before transferring it to magnetic tape via the DESY IBM 370/168 computer.

The trigger rate was about ten trigger per 10^6 tagged quanta. The intensity of 2-4 x 10^5 tagged quanta per second was limited by the rates of the tagging system and the single rates in the front proportional chambers, which were irradiated by a large flux of pairs and Compton electrons. The multiwire proportional chambers showed an accidental hit in every third or 4th strobe, which could be used for monitoring the beam position.

3e Data Reconstruction

We identified in a first step particle trajectories using a pattern recognition program[8] taking events from our raw data sample carrying a unique tagging information.

With the help of a track fitting procedure two prong events have been reconstructed simultaneously in both projections, using the corresponding signals identified in the multiwire-proportional- and spark chambers. The fit rendered particle momenta and the vertex coordinates.

Fig. 5 shows orthogonal projections of reconstructed interaction points together with the physical boundaries of the target.

The Cerenkov information identified outgoing particles above threshold with a high probability as K mesons.

Since the energy of the incoming gamma is also known, one can compute the missing mass and plot the invariant mass of the measured $K^{\pm}$-pair versus the mass of the recoil system. A two dimensional plot for invariant K^+K^- mass versus recoil mass is shown in fig. 6, where the elastic ϕ signal shows up clearly.

Due to the association of the ϕ with higher recoil masses there is clear evidence for inelastic ϕ production.

This evidence was confirmed through the recoil hodoscope, by which it could be proved, that the 'inelastic events' are not elastic events with a falsly assigned gamma-energy.

The kinematic separation of elastic from inelastic events could be obtained by selecting events which fell in both mass bands, the invariant K^+K^- mass around the

ϕ meson ($1.01 \leq M_{KK} \leq 1.03$ GeV) and the recoil mass around the proton ($0 \leq M_X \leq 1.15$ GeV). The invariant K^+K^- distribution for a recoil mass in the proton band is shown in fig. 7.

As an alternative method for the kinematic separation we fitted the two prong events applying the energy momentum constraint (1c fit).

A probability distribution for the 1c kinematic fit is shown in fig. 8. From this distribution we selected elastic events with a confidence level of 0.95. Both methods gave essentially the same results.

The experimental width of the recoil proton peak (110 MeV FWHM) and of the ϕ mass peak (7 MeV FWHM) is consistent with our experimental momentum and energy resolution: $\sigma(p_{K^\pm}) \simeq 0.01 \cdot p_{K^\pm}$ for $p = 3$ GeV and $\sigma(E_\gamma) = 25$ MeV.

As a test for both the mass resolution and the calibration of the mass scale we analyzed a $K^o \to 2\pi$ signal in our raw data sample. The invariant mass of two-prongs was evaluated, where the momenta of both particles were below the Cerenkov threshold for pions and the interaction points were downstream of the end window of the target.

The result is shown in fig. 9, where one recognizes the signal $K_s^o \to \pi^+\pi^-$ with a mass resolution of 6 MeV.

For the evaluation of the differential cross section $\frac{d\sigma}{dt}$ ($\gamma p \to \phi p$) the elastic data sample has been subjected to the following conditions:

- all cuts with respect to charge, geometric boundaries and trigger conditions were applied again in the off line analysis to the elastic data sample;
- the momenta of both particles had to be above Cerenkov threshold;
- to each event we assigned a detection efficiency which was computed with Monte Carlo technics, corresponding to the photon energy E_γ and the four momentum transfer t (see § 4a). Events with detection efficiencies below 0.03 were rejected.

§4. Differential Cross Section of the Elastic ϕ Production

4a Corrections

The differential cross section has been evaluated for bins Δt_i

$$\frac{d\sigma}{dt_i} = \frac{R_i}{F_i \cdot \Delta t_i} \cdot \frac{\varepsilon}{n} \quad , \tag{4.1}$$

with $R_i = N_i W_i$, where N_i is the number of events in the i^{th} energy- and t bin after background has been subtracted, W_i is a weight associated with each event calculated by Monte Carlo technics, F_i is the number of incident photons in the i^{th} energy bin corrected for the bremsstrahlung distribution based on the counting rate in the seven big tagging channels, Δt_i is the bin size of the four-momentum transfer squared. The quantities n and ε are independent of the individual events: $n = \rho L_o \ell / A$ is the number of protons per cm^2, where ρ is the liquid hydrogen density, L_o is Loschmidt's number, ℓ is the target length and A is the atomic weight of hydrogen (in gram). ε is a product of energy- and t-independent correction factors which are given below:

- losses due to knock-on electrons produced by a kaon in the window or radiator of the Cerenkov counter:	1.09 ±0.02
- losses in the track recognition procedure:	1.04 ±0.01
- losses due to the momentum and vertex reconstruction program:	1.12 ±0.02
- losses due to multiprong events:	1.035±0.01
- losses due to single rate of the Cerenkov counter (veto rate):	1.02 ±0.01
- losses due to hadronic interaction of hadrons in the target and scintillation counters:	1.02 ±0.01
- losses due to counter inefficiencies:	1.01 ±0.01
- correction for tagging efficiency and zeros and multiples in the small tagging counters:	1.28 ±0.02
- correction for the branching ratio $BR(\phi \to K^+K^-/\phi \to all)$:	2.14

The overall correction factor c and its systematic error is thus 3.78 ± 0.14 which amounts to a 4 % systematic error.

For the determination of $\frac{d\sigma}{dt}$ the t and E_γ dependent correction factors W_i have been computed using Monte Carlo technics. The following effects have been taken into account: the transverse distribution of the photon beam, the multiple scattering and nuclear absorption in all materials, energy loss in the target, the decay in flight of the kaon including corrections for the possibility that the secondaries from K decay cause a Cerenkov signal, the effective geometric and triggering acceptance and kaon momentum cuts.

It was assumed that the decay angular distribution of the ϕ meson has a $\sin^2\theta$ shape, where θ is the polar angle of K^+ in the helicity frame. This assumption was confirmed experimentally. For further discussion see §5.

4b Analysis of the elastic cross section

About 4500 events in the energy range from 3.0 to 6.7 GeV have been selected falling in K^+K^- mass bins $1.01 \leq M_{KK} \leq 1.03$ GeV and in the recoil mass range $M_X \leq 1.15$ GeV. Using the methods and corrections described in § 4a we obtained elastic differential cross sections which are presented in fig. 10 and table 3. The straight lines in fig. 10 are best fits to the data using an exponential form

$$\frac{d\sigma}{dt} = \left(\frac{d\sigma}{dt}\right)_{t=0} \exp\left(-B\,|t|\right) \qquad (4.2)$$

The best fit values for the extrapolated forward cross sections to $t = 0$ $(d\sigma/dt)_o$ and the slope value B are listed also in table 3.

Whereas the cross section measurements of this experiment agree with other measurements in overlapping t regions ($|t| \approx 0.4$ GeV^2) a significant steepening of the differential cross section was observed at forward direction.

The slopes of our experimental t-distributions are found to be significantly larger than those reported by previous ϕ photoproduction experiments [2] which in most cases did not cover the small t-region. This fact is substantiated by the single energy measurement of the Cornell group [*] in the same t-region as this experiment.

The extrapolated cross section intercepts (optical points) $\left.\frac{d\sigma}{dt}\right|_o$ at our energy range show an energy dependence. In fig. 11 $\left.\frac{d\sigma}{dt}\right|_o$ is plotted as a function of E_γ together with values obtained in other experiments [2]. A simple explanation for this energy dependence can be found in applying the VDM relation (2.4).

If one assumes that

$$C = \frac{\alpha}{64\pi} \cdot \frac{4\pi}{\gamma_\phi^2} \cdot (1+\eta_\phi)^2 \cdot \sigma_{tot}^2 (\phi p) \qquad (4.3)$$

is constant in our energy range, we can fit the optical points of this experiment (including the threshold point) to the relation

$$\left(\frac{d\sigma}{dt}\right)_o = C \cdot \left(\frac{p_\phi}{k}\right)^2_{CM} . \qquad (4.4)$$

We obtained the result (fig. 11) $C = (2.93 \pm 0.08)\ \mu b/GeV^2$.

This result explains the energy dependence of our data and is in excellent agreement with all other published optical points in this energy range. In addition it supports the assumption that $(1+\eta_\phi^2)\sigma^2_{tot}(\phi p)$ is essentially energy independent in the energy range considered.

Furthermore, since the product of $(\gamma_\phi^2/4\pi)^{-1}$ and $\sigma_{tot}(\phi p)$ is fixed by the above value of C (for η we used the value 0.06 determined in a recent experiment [9]), our experiment establishes a correlation between the γ_ϕ coupling constant and $\sigma_{tot}(\phi p)$ which can be compared to values of $\sigma_{tot}(\phi p)$ and $\gamma_\phi^2/4\pi$ obtained both with different methods and in other experiments. Fig. 12 shows the curve which corresponds to the C value obtained in this experiment. The plot shows also the e^+e^- annihilation value for $\gamma_\phi^2/4\pi$ [10] and of $\sigma_{tot}(\phi p)$ obtained by ϕ photoproduction on C^{12} (Ref. 2 (D-MIT)).

In addition figure 12 shows upper and lower bounds of $\sigma_{tot}(\phi p)$ by computing quark sum rules for $\sigma(\phi p)$ from total hadronic cross sections extrapolated from NAL energies into the 2-10 GeV region [11].

4c The slope of the pomeron

The analysis of the ϕ cross section yields information on the properties of the pomeron trajectory as discussed in §2. Because of the observed t-dependence of the slope B the analysis of the pomeron slope was confined to the forward region of the differential cross section.

Using only data with $t \leq 0.4$ GeV^2, all available experimental results *) have been refitted to the form $A \exp(-B|t|)$. Fig. 13 and table 4 present the results of these fits. The straight lines in fig. 13 are the best fit to the form

$$B = b + 2\alpha'(0) \cdot \ln(s/s_0) \quad , \tag{4.5}$$

with $b = 4.2 \pm 1.4$ GeV^{-2} and $\alpha'(0) = 0.27 \pm 0.29$ GeV^{-2}, which is essentially consistent with 'no shrinkage'. This result is consistent with that at $t = 0.6$ GeV^2 obtained by combined cross sections from SLAC and Bonn data **).

The significance of this result is limited since we only used data in a comparatively small s region. For hadron induced reactions at FNAL-energies the slope value [12] of the pomeron trajectory was obtained to $\alpha'(0) \simeq 0.2$ GeV^{-2} at $t = 0.2$ GeV^2.

In order to improve the statistics and to increase the energy range, the world data on ϕ photoproduction were grouped into three energy bins as shown in table 5. In each bin the slope value of the differential cross section was evaluated at $t = 0.2$ GeV^2 by fitting the data over the whole t-region to the form $\frac{d\sigma}{dt} \propto \exp(a\,t + bt^2)$. The result is given in table 5 and plotted in fig. 14 together with the result from ref. 15. Here the authors have computed the cross section using the SU(3) relation with ideal mixing from elastic cross sections of πp and kp scattering at FNAL energies. Thus the slope value obtained from the photoproduction data is consistent to that derived from the hadronic reactions. By fitting the points in fig. 14 to the form (4.5), one gets $b = 4.66 \pm 0.22$ GeV^{-2} and $\alpha'(0) = 1.19 \pm 0.02$ GeV^{-2}. The solid curve in fig. 14 is based on the fitted values.

§5. Spin Density Analysis in the ϕ Region

The geometric acceptance of our experimental set up has a reasonable efficiency for the entire range of the polar decay angle θ of the kaon measured in the K^+K^- restsystem. Hence for kinematic reconstructed events it was possible to study the spin structure of the K^+K^- system, in particular to evaluate spin density matrix elements of the ϕ as a function of the four momentum transfer t and E_γ.

For the evaluation of the spin density matrix elements ρ_{ik} we applied two essentially equivalent methods:

(i) For the ϕ being a spin 1 resonance which decays into two spinless particles (kaons), the decay distribution can be expressed in terms of the spin density elements ρ_{ik} as follows [13]

$$I(\Theta,\phi) = \frac{3}{4\pi}\left\{\rho_{00}\cos^2\Theta + \rho_{11}\sin^2\Theta - \rho_{1-1}\sin^2\Theta\cos 2\phi - \sqrt{2}\,\mathrm{Re}(\rho_{10})\sin 2\Theta\cos\phi\right\} \qquad (5.1)$$

$$\rho_{00} = 1 - 2\,\rho_{11}$$

where θ and ϕ are the polar and azimuthal decay angles of the K^+ in the restsystem of the ϕ. I is normalized with the total number of events.

The experimental data have been fitted to the relation (5.1) by optimizing the parameters ρ_{ik} using least square and likelihood methods.

(ii) The ρ_{ik} have also been evaluated by computing numerically moments of spherical harmonics $\langle Y_L^M \rangle$ from the acceptance corrected experimental decay distribution $I_c(\theta,\phi)$, normalized to the total number of events:

$$\frac{\langle Y_L^M \rangle}{\langle Y_0^0 \rangle} = \int I_c(\Theta,\phi)\; Y_L^M(\Theta,\phi)\; d\Omega \qquad (5.2)$$

The ρ_{ik} for J=1 are then related to the moments in the following way:

$$\rho_{00} = \frac{1}{3}\left(\sqrt{5}\,\frac{\langle Y_2^0\rangle}{\langle Y_0^0\rangle} + 1\right)$$

$$\rho_{1-1} = -\sqrt{\frac{5}{6}}\,\mathrm{Re}\,\frac{\langle Y_2^2\rangle}{\langle Y_0^0\rangle} \qquad (5.3)$$

$$\mathrm{Re}(\rho_{10}) = \sqrt{\frac{5}{12}}\,\mathrm{Re}\,\frac{\langle Y_2^1\rangle}{\langle Y_0^0\rangle}$$

The decay angular distributions have been studied with respect to two reference frames. In the s-channel or helicity (H) system the axis of quantisation corresponds to the direction of the outgoing phi as seen in the overall center of momentum system. In the t-channel or Gottfried-Jackson (G-J) system [14] the axis of quantisation corresponds to the direction of the incident photon as seen in the phi meson restsystem (see figure 15).

By convention the angle between the direction of the K^+-meson and the z-axis is the helicity polar angle θ and the angle between the x-axis and the projection of the K^+ direction on the xy-plane is the heliciy azimuthal angle.

Experimental efficiencies, related mainly to geometric and decay in flight losses, have been computed with Monte Carlo technics for a multidimensional grid of the kinematic variables ($M_{K^+K^-}$, E_γ, t, θ, ϕ). Inverse efficiencies were used as weight factors for the experimental events grouped in corresponding bins.

Using the methods described before we evaluated density matrix elements ρ^H_{ik} and ρ^{GJ}_{ik} referring to both coordinate systems, the H resp. G-J frames.

The kinematic regions of this analysis were

$$1.01 \leq M_{K^+K^-} \leq 1.03 \text{ GeV},$$

$$4.66 \leq E_\gamma \leq 6.70 \text{ GeV} \quad (2 \text{ bins}),$$

$$0 \leq |t - t_{min}| \leq 0.2 \text{ GeV}^2 \quad (4 \text{ bins}).$$

The results which we obtained from the different fitting procedures were consistant within the errors. The results are listed in tables (6a) and (6b) and plotted in figs. 16a and 16b.

For conservation of the s-channel helicity (SHC) one expects for photoproduced ϕ mesons a $\sin^2\theta^H$ distribution of the decay in the H-frame which is independent of t. The experimental decay distribution of the ϕ showing a $\sin^2\theta$ shape confirms SHC (see fig. 17, $1.01 \leq M_{KK} \leq 1.03$ GeV). ρ^H_{oo} is essentially zero in the t range considered whereas the corresponding element in the G-J-frame shows a clear t dependence.

The fact that the offdiagonal elements ρ^H_{1-1}, Re ρ^H_{10} which are related to spin-flip contributions in the ϕ production show slight deviations from zero, indicates the presence of other than SHC-amplitudes contributing to the K^+K^- spectrum. In particular the significant deviation of ρ^{GJ}_{10} from zero represents the presence of unnatural parity exchange (see §6 and §7).

§6. Helicity Amplitudes for Diffractive ϕ Photoproduction

The density matrix elements and the differential cross section evaluated in this experiment have been used to carry out an analysis of the helicity amplitudes which contribute to the ϕ photoproduction.

This analysis is based on a Regge model for the photoproduction and decay of vector mesons which was developped by P. Schlamp [15] and has been used by I. Derado et al. [16] for an analysis of ρ^o photoproduction. The model is restricted to the exchange of even signature, natural parity trajectories. (For details of the model see ref. 18). The t-channel helicity amplitudes are then defined by

$$f^t_{\lambda_\phi \lambda_\gamma \lambda_{\bar{p}} \lambda_p} = \gamma_{\lambda_\phi \lambda_\gamma \lambda_{\bar{p}} \lambda_p}(t)\, b_{\lambda\mu}(t)\, \frac{1+e^{-i\pi\alpha(t)}}{\sin \pi\alpha(t)} \left(\frac{s}{s_0}\right)^{\alpha(t)-\lambda_{max}}, \qquad (6.1)$$

with scaling constant $s_o = 1\ \mathrm{GeV}^2$, $\lambda = \lambda_{\bar{p}} - \lambda_p$, $\mu = \lambda_\phi - \lambda_\gamma$ and $\lambda_{max} = \mathrm{MAX}(|\lambda|, |\mu|)$. The terms $b_{\lambda\mu}(t)$ take into account kinematic and Regge singularities and contain also dimension factors to make the amplitudes dimensionless.

$\gamma_{\lambda_\phi \lambda_\gamma \lambda_{\bar{p}} \lambda_p}(t)$ which is proportional to the residue function has been parametrized as follows:

$$\gamma_{\lambda_\phi \lambda_\gamma \lambda_{\bar{p}} \lambda_p}(t) = g \cdot \exp(-a|t| - bt^2) \cdot r_{\lambda_\phi \lambda_\gamma \lambda_{\bar{p}} \lambda_p} \qquad (6.2)$$

where constants g, a and b depend on the exchange trajectory $\alpha(t)$. The $r_{\lambda_\phi \lambda_\gamma \lambda_{\bar{p}} \lambda_p}$ are constants depending only on the helicity states of incoming and outgoing particles.

In our analysis only the pomeron exchange was considered. Hence $\alpha(t)$ was parametrized as

$$\alpha(t) = 1 + \alpha'(o)t \quad .$$

As far as the helicity dependent constants are concerned, only three of them are free parameters, $r_{1\ 1\ 1/2\ -1/2}$, $r_{0\ 1\ 1/2\ -1/2}$ and $r_{-1\ 1\ 1/2\ 1/2}$, because of the overall normalization g one can set $r_{1\ 1\ 1/2\ 1/2} = 1$). Thus we get six independent helicity amplitudes in the t-channel using the free parameters above. The explicit form of the amplitudes (6.2) can be found in ref. 18.

The physical quantities, i. e. the differential cross sections and the density matrix elements are related to these amplitudes in the following way:

$$\frac{d\sigma}{dt} = \frac{1}{8\pi (s-M^2)^2} \sum_{\lambda_\phi \lambda_\gamma \lambda_{\bar{p}} \lambda_p} f^t_{\lambda_\phi \lambda_\gamma \lambda_{\bar{p}} \lambda_p} \cdot f^{t\,*}_{\lambda_\phi \lambda_\gamma \lambda_{\bar{p}} \lambda_p} \tag{6.3}$$

$$\rho^H_{\lambda_\phi \lambda'_\phi} = \frac{1}{N} \sum_{\lambda_{p'} \lambda_\gamma \lambda_p} f^s_{\lambda_\phi \lambda_{p'} \lambda_\gamma \lambda_p} \cdot f^{s\,*}_{\lambda'_\phi \lambda_{p'} \lambda_\gamma \lambda_p} \tag{6.4}$$

$$\rho^{G-J}_{\lambda_\phi \lambda'_\phi} = \frac{1}{N} \sum_{\lambda_{\bar{p}} \lambda_p \lambda_\gamma} f^t_{\lambda_\phi \lambda_\gamma \lambda_{\bar{p}} \lambda_p} \cdot f^{t\,*}_{\lambda'_\phi \lambda_\gamma \lambda_{\bar{p}} \lambda_p} \tag{6.5}$$

$$N = \sum_{\lambda_\phi \lambda_{p'} \lambda_\gamma \lambda_p} f^s_{\lambda_\phi \lambda_{p'} \lambda_\gamma \lambda_p} \cdot f^{s\,*}_{\lambda_\phi \lambda_{p'} \lambda_\gamma \lambda_p} \tag{6.6}$$

where sufficies H and GJ denote helicity frame and Gottfried-Jackson system, respectively. The helicity amplitudes for the s-channel $f^s_{\lambda_\phi \lambda_{p'} \lambda_\gamma \lambda_p}$ are obtained by means of the crossing relation [17] from $f^t_{\lambda_\phi \lambda_\gamma \lambda_{\bar{p}} \lambda_p}$ (See eq. (17) in Ref. 18).

By fitting eq. (6.4) to the experimental density matrix elements in the helicity frame, three sets of the helicity dependent constants $r_{\lambda_\phi \lambda_\gamma \lambda_{\bar{p}} \lambda_p}$ have been evaluated by making assumptions about α'. The three cases considered are:

(A) $\alpha'(0) = 0.22\ \text{GeV}^{-2}$ from the pp result [18],

(B) $\alpha'(0) = 0.27\ \text{GeV}^{-2}$ from the result in equation (4.4), and

(C) $\alpha'(0)$ = free parameter.

The results are listed in table 7a for each case [19].

Using the parameter set obtained for the case (A), the parameters g, a and b were obtained by fitting eq. (6.3) to a compilation of all published ϕ data [2]. Here again we distinguish 2 cases:

(D) g, a and b are free parameters,

(E) g and a are free parameters and b = 0.

The fitting results are listed in table 7 b.

The ρ^H_{ik} calculated theoretically on the basis of (6.4) for the case (A) are plotted in fig. 18 as solid curves passing through the experimental values of ρ^H_{ik}. The corresponding density matrix elements in the Gottfried-Jackson system from eq. (6.4) are also given by the solid curves in fig. 18, together with the experimental points.

The theoretical cross sections due to eq. (6.3) fitted for the assumptions (D) and (E) are drawn in fig. 19. In this figure, an experimental curve fitted with data only for $|t| > 0.4$ GeV^2 is presented for a comparison with experimental results for $|t| \leq 0.4$ GeV^2.

The helicity amplitudes evaluated for the assumptions (A) and (D) for both s- and t-channels are plotted in fig. 20. For a comparison, the corresponding helicity amplitudes for ρ^o photoproduction obtained by Derado et al. [*] are shown as broken lines after being normalized to the scale of the ϕ photoproduction amplitudes.

One notices that the imaginary part of the s-channel helicity conserving amplitude $f_1 \equiv f_{1\ 1/2\ \ 1\ 1/2}$ is the most dominant one. There are however also small contributions from s-channel helicity non-conserving amplitudes.

This model yields also an information on the ratio of the real to imaginary part η of the SHC-amplitudes f_1: η is substantially smaller in phi photoproduction as compared to rho photoproduction in the entire t range considered (see fig. 21).

§7. Spin Parity Structure of the KK System outside of the ϕ

The angular momentum structure of the K^+K^- system has been studied also outside of the ϕ mass by analyzing the K^+ angular distribution in the K^+K^- helicity frame as a function of the K^+K^- invariant mass. The most notable feature is a dramatic change of the K^+K^- angular distribution when one passes over the ϕ mass region (see fig. 17). The $\sin^2\theta_H$ distribution in the ϕ region changes abruptly in character going to larger KK masses, exhibiting a distribution which has predominantly a $\cos^2\theta_H$ dependence. Taking a $t-t_{min}$ range from 0 to 0.20 GeV^2 and mass bins ΔM_{KK} = 0.01 GeV, we computed moments of spherical harmonics of the M_{kk} angular distribution in the helicity frame using the relation

$$\langle Y_L^M \rangle = \sum_i W_i \, (\theta_i^H, \phi_i^H, M_{KK}) \; Y_L^H(\theta_i^H, \phi_i^H) \qquad (7.1)$$

W_i is the acceptance corrected event rate in the angular and mass bin considered.

For each mass bin the acceptance weights have been evaluated using Monte Carlo technics. In fig. 22 we plotted the normalized moments $\langle Y_L^M \rangle / \langle Y_o^o \rangle$ as a function of M_{KK}. The spectra of the moments above the ϕ exhibit in general a very smooth dependence on the KK mass, which is an indication that the number of amplitudes contributing there to the KK final state is not large.

The moment for L=2, M=0, representing the helicity conserving part of the spin 1 amplitude, shows a negative bump at the ϕ mass. It crosses the zero line already at M_{KK} = 1.05 GeV increasing almost smoothly to large positive values. Small wiggles also in higher moments between M_{KK} = 1.06 GeV and M_{KK} = 1.1 GeV might indicate the presence of interfering resonant partial waves. The odd integer moments are practically always zero. A small signal of $\langle Y_1^o \rangle$ below the ϕ mass which disappears at the ϕ mass can be interpreted as an interference between the helicity non conserving part of the ϕ production and the presence of the $S_{993}(0^+)$ meson. Although the KK mass distribution shows no direct evidence of the presence of S_{993}, the clear interference signal was the basis for an analysis to estimate limits for the photoproduction cross section of the S_{993} meson $\to K^+K^-$. Assuming the width and mass reported in the Table of Particle Properties we estimate an upper limit for the cross section of this reaction:

$$\sigma\ (\gamma p \to p S_{993} \to p K^{+} K^{-}) \leq 2.7 \pm 1.5\ \text{nb} \quad .$$

From the amplitude analysis we obtained the result that the assumption of a real amplitude for the production of a resonant state at M_{KK} = 993 MeV is well consistant with the data. For details of the analysis and results see ref. 20.

§8. The Inelastic ϕ Production

By eliminating events due to reaction (1.1) a substantial sample $\phi \to K^+K^-$ events remained, which failed to fit the elastic hypothesis $\gamma + p \to K^+ + K^- + p$. Hence the remaining events are of the inelastic type

$$\gamma + p \to \phi + X \to K^+ + K^- + X \quad , \tag{8.1}$$

where X denotes a missing mass different from the proton mass.

The evaluation of the differential cross section of the inelastic reaction with respect to both, the missing mass M_x and $t-t_{min}$, needed a careful study of the acceptance corrections of the experimental apparatus, and of the background subtraction under the ϕ. In the Monte-Carlo-calculation of the effective detection efficiency for reaction (8.1) the following effects have been taken into account, in addition to the effects already considered for the elastic data, and were used as corrections in the off-line analysis:

- The momenta of the decay kaons are for kinematic reasons lower than in the case of elastic data. Thus the decay in flight corrections are of greater importance, in particular because muons from K-decay can cause a vetosignal in the Cerenkov counter.
- Fast pions from the bulk of the inelastic final states can in general hit the Cerenkov counter and generate an antisignal.
- The front counters (F) will frequently be triggered by inelastic final state particles. This effectively constitutes an enlarged trigger acceptance for inelastic data.
- Multiprong events, not recognized or considered in the analysis procedure, may contribute to reaction (8.1).

The inelastic sample has been selected by cutting the distribution of the invariant K^+K^- mass M_{kk} around the ϕ mass region, $1.01 \leq M_{kk} \leq 1.03$ GeV and demanding the missing mass $M_x \geq 1.20$ GeV. The events were taken from an energy range $4.6 \text{ GeV} \leq E_\gamma \leq 6.7$ GeV. This mass cut is equivalent within our uncertainties to a selection on the basis of a kinematic one constraint fit if we demand that the fit proba-

bility for the elastic hypothesis is smaller than 0.001, see fig. 8. The regions of missing mass and momentum transfer squared are given by $1.20 \leq M_X \leq 2.10$ GeV and $0 \leq |t-t_{min}| \leq 0.2$ GeV^2, respectively.

Fig. 23 shows the K^+K^- invariant mass distribution due to reaction (8.1) for 4 different energy ranges. The ϕ signal appears on top of a broad K^+K^- background which rises steeply from threshold and becomes rather flat in the mass region above the ϕ. The missing mass M_X corresponding to the ϕ signal was taken from 1.2 to 2.1 GeV.

We applied two different procedures to evaluate the inelastic ϕ cross section:
In a cut a) (Fig. 23) we required both K momenta to be larger than 1.8 GeV, thus reducing the background dramaticly but not the ϕ-peak. In order to compute acceptance weights for this cut assumptions have to be made about the decay angular distribution of inelasticly produced ϕ mesons.
For cut b) (Fig. 23) the ϕ signal was obtained by fitting in the upper curves a Gaussian and a polynomial to the ϕ signal and the background, respectively.
Both methods may introduce certain biases:
cut a), because the assumption about the angular distribution can influence the acceptance weights
cut b), because the shape of the background polynomial near threshold determines to some extend the size of the signal.
The results obtained by the two methods were in agreement within 20 %.
The plots and numerical results given in this paper are based on the cut b).
The errors quoted are statistical ones. A systematic uncertainty of about 20 % on the cross section can not be excluded.

Double differential cross sections with respect to $t-t_{min}$ have been evaluated for 3 mass bins ΔM_X by computing corresponding acceptance weights with Monte Carlo technics (fig. 24).

Differential cross sections integrated over the mass range $1.2 < M_X \leq 2.1$ for different γ-energies are plotted in fig. 25 and listed in table 8.

An exponential of the form

$$\frac{d\sigma}{d|t-t_{min}|} = \left.\frac{d\sigma}{dt}\right|_{t=t_{min}} \cdot \exp\left(-B|t-t_{min}|\right) \qquad (8.2)$$

was fitted to the data. Table 8 lists the intercepts $\left.\frac{d\sigma}{dt}\right|_{t=t_{min}}$, the slope B, and the signal-over-background-ratio for 4 energy bins.

One notices that the inelastic data show in general a flater t distribution and a relatively large cross section. In particular there is evidence that the slope becomes smaller with increasing M_X. This is shown on fig. 26 were the slope is plotted versus M_X together with results from $K^+p \to K^+X$ [21].

For a comparison of elastic and inelastic ϕ-production one can consider the ratio of total cross sections

$$\frac{\sigma^{inel}\ (\gamma p \to \phi X)}{\sigma^{el}\ (\gamma p \to \phi p)} \qquad X \neq p \tag{8.3}$$

Since due to the limited acceptance of our set up only a part of the total cross sections was recorded and since the t slope for large t-values is not known we have plotted in fig. 27 the ratio

$$\left.\frac{d\sigma^{inel}\ (\gamma p \to \phi x)}{d|t-t_{min}|} \Big/ \frac{d\sigma^{el}\ (\gamma p \to \phi p)}{d|t-t_{min}|}\right|_{t=t_{min}} \tag{8.4}$$

which has been determined in our experiment and carries an information related to (8.3). The comparatively strong inelastic signal of vector mesons in photoproduction has also been observed in the photoproduction of ρ^o mesons for photon energies from 4 to 18 GeV [22].

Acknowledgement

We gratefully acknowledge the support of the synchrotron-operator crew, the floor service and the computing center. We thank Dr. V. Böhmer, Mr. A. Krolzig and his group, our technicians V. Wesche, W. Burmester and A. Höhne and our students W. Hagen, D. F. Jarowoy, K. LeVrang and W. Ziekursch for technical support and assistance. Dr. F. E. Taylor helped us in an early stage of the experiment and designed the tagging system. The Karlsruhe group wishes to express their gratitude to DESY for hospitality and acknowledges the financial support of the Kernforschungszentrum Karlsruhe and the Bundesministerium für Forschung und Technologie.

FOOTNOTES

Footnotes Page 4

* The f meson decays predominantly into pure pion final states, $BR(f\to 2\pi/f\to all) = 0.81 \pm 0.01$, $BR(f\to 4\pi/f\to all) = 0.028 \pm 0.003$, $BR(f\to K\bar{K}/f\to all) = 0.027 \pm 0.006$ (see Rosenfeld tables and [5]).

** The decay branching ratio of the f' meson is not accurately known. It will not entirely decouple from $\bar{p}p$. By considering its mass and spin, the intersecting point of the P'' trajectory would be smaller than $\alpha_f(0) = 0.41$ [6].

Footnote Page 14

* The authors of (C-72) in ref. 2 gave the slope value 5.4 ± 0.3 GeV^{-2} assuming a linear exponential form of the t-distribution in $0.08 \leq t \leq 0.52$ GeV^2.

Footnotes Page 16

* Experimental values for $d\sigma/dt$ have been obtained through privat communication for all but (S-W) in ref. 2. The data of (S-W) have been taken from their graph.

** See (BONN) and (S-W) in ref. 2.

Footnote Page 22

* The authors of ref. 16 used the value 0.5 GeV^{-2} for the slope of the pomeron trajectory.

REFERENCES

1. H.-J. Behrend et al., Phys. Letters 56B (1975) 408.

2. (D-BC) ABBHHM, Phys. Rev. 175 (1968) 1669,
(S-CT) R. L. Anderson et al., Phys. Rev. D1 (1970) 21, and
D. L. Kreinick, PhD Thesis, California Institute of Technology, 1969 (unpublished),
(D-MIT) H. Alvensleben et al., Phys. Rev. Letters 28 (1972) 66,
(C-72) C. Berger et al., Phys. Letters 39B (1972) 659,
(C-71) G. McClellan et al., Phys. Letters 26 (1971) 1593,
(S-W) R. L. Anderson et al., Phys. Rev. Letters 30 (1973) 149,
(S-B-T) J. Ballam et al., Phys. Rev. 7D (1973) 3150,
(BONN) H. J. Besch et al., Nucl. Phys. B70 (1974) 254,
(D-K) This experiment.

3. H. Joos, Phys. Letters 24B (1967) 103;
P. G. O. Freund, Nuovo Cimento 48 (1967) 541;
V. Barger and D. Cline, Phys. Rev. Letters 24 (1970) 1313.

4. S. Okubo, Phys. Letters 5 (1963) 165;
G. Zweig, CERN Report No. TH. 412, 1964 (unpublished);
I. Iizuka, Prog. Theor. Phys. Suppl. 37-38 (1966) 21.
D. Cohren, D. S. Ayres, R. Diebold, S. L. Kammer, A. J. Pawlicki and A. B. Wicklund, Phys. Rev. Letters 38 (1977) 269.

5. W. Wentzel et al., Nucl. Phys. 115B (1976) 208.

6. C. Quigg and E. Rabinovici, Phys. Rev. D13 (1976) 2825.

7. F. J. Gillman, J. Pumplin, A. Schwimmer and L. Slodosky, SLAC-719, 1970.

8. H. Hirschmann, Kernforschungszentrum Karlsruhe, KFK 2209 (1975).

9. S. Bartalucci et al., DESY 77/56, 1977.

10. D. Benaksas et al., Phys. Lett. 39B (1972), 289,
D. Benaksas et al., Phys. Lett. 42B (1972), 507.

11. D. Joynson, B. Nicolescu, Lab. de Physique Théorique des Particules Elémentaires Université Pierre et Marie Curie Paris. IPNO/TH 75-3,
M. Krammer Acta Phys. Austriaca 32 (1970), 395.

12. D. S. Ayres et al., Phys. Rev. D15 (1977) 3105.

13. W. Koch in Analysis of Scattering and Decay edited by M. Nicolic (Gordon and Breach Science Publishers INC, New York, 1968).

14. J. D. Jackson, Nuovo Cimento 34 (1964) 1644.

15. P. Schlamp PHD-Thesis, Univ. München 1971.

16. I. Derado, G. Kronseder, P. Schacht and P. Schlamp, Nucl. Phys. D38 (1972) 541.

17. L. L. Wang, Phys. Rev. 142 (1966) 1187.

18. A. Martin, Nucl. Phys. B77 (1974) 226.

19. D. Heine, Kernforschungszentrum Karlsruhe KFK 2284, 1976.

20. D. C. Fries et al., to be submitted to Nucl. Phys. B.

21. R. K. Carnegie et al., Physics Lett. 59B (1975) 313.

22. A. Silverman, proceedings of the 1975 Intern. Symp. on Lepton and Photon Interactions at High Energies, Stanford Univ. 1975, Editor W. T. Kirk.

23. D. C. Fries, Proceed. of the Sixth Recontre de Moriond. Editor I. Tran Thanh Van, Orsay 1971, 267.

24.. E. Kogan et al., Nucl. Phys. B122 (1977) 383.

Table Captions

1. A summary of specifications of components used in this experiment, (a) for Exp I, (b) components changed in (a) for Exp II and Exp III.

2. A summary of the energy ranges used in these experiments.

3. The elastic differential cross sections in $\mu b/GeV^2$. The optical points and the slope values are fitted values assuming a linear exponential t-dependence.

4. Fitted slope values obtained for other ϕ photoproduction experiments with a linear exponential fit to the limited range $|t| \leq 0.4\ GeV^2$.

5. Fitted slope values at $t = 0.2\ GeV^2$ of several experiments referenced in 2).

6. The spin density matrix elements for the elastic data, (a) in the helicity- and (b) in the Gottfried-Jackson frame.

7. Fit parameters of the helicity amplitudes for different assumptions described in §6.

8. Table of the inelastic differential cross sections versus $t-t_{min}$ integrated over 1 GeV mass range in $\mu b/GeV^2$ for 4 different photon energy regions. The slope values were obtained by assuming a linear exponential form of the t-distribution.

Table 1 a

Device	No.	Dimension	Comment
Tagging small counter	22	0.5 x 4 x 1.7 to 19.4 cm^3.	
Tagging large counter	14	1 x 4 x 12 to 45 cm^3.	thick x wide x long
Recoil counter	23	0.5 x 3.3 x 57.5 cm^3.	
Front counter	4	0.5 x 15 x 15 cm^3.	2.5 cm ϕ hole about beam axis
Back A-counter	4	1 x 30 x 100 cm^3.	
Back B-counter	5	1 x 30 x 100 cm^3.	
Cerenkov counter	1	entrance window 1.0 x 2.1 m^2 (height x width), viewed by six photomultipliers.	threshold was 1.6 GeV/c for pions.
Multiwire prop. chamber	2	30 x 30 cm^2, 60 x 60 cm^2 (wide x long)	wire space = 2 mm
Spark chamber	8	1×1 m^2, the first two chambers were rotated by 45°.	wire space = 2 mm
Target center and front surface of beam stopper		2168 mm, 786 mm from the center of magnet, respectively.	

Table 1 b

Device	No.	Dimension	Comment
Front counter	16	0.5 x 2 x 30 cm^3	2×2 cm^2 hole about beam axis
Middle counter	12	0.5 x 12 x 75 cm^3 thick x wide x long	
Multiwire prop. chamber	1	60 x 60 cm^2	wire space = 2 mm
Target center and front surface of beam stopper		1420 mm, 185 mm from the center of magnet, respectively.	

Table 2

Period	Electron Energy	Photon Energy
Experiment I	7.2 GeV	4.65 - 6.70 GeV
Experiment II	5.5 GeV	3.0 - 5.0 GeV
Experiment III	5.2 GeV	3.0 - 4.5 GeV

TABLE 3

$\|t\|$ GeV^2	Incident photon energy (GeV)						
	3.0 - 3.5	3.5 - 4.0	4.0 - 4.5	4.5 - 5.1	5.1 - 5.6	5.6 - 6.2	6.2 - 6.7
0.01							2.63 ± 0.21
0.03		1.51 ± 0.23	1.44 ± 0.17	1.76 ± 0.12	1.86 ± 0.14	2.06 ± 0.16	2.20 ± 0.18
0.05	1.19 ± 0.13	1.36 ± 0.71	1.42 ± 0.21	1.69 ± 0.14	1.75 ± 0.16	1.65 ± 0.16	1.96 ± 0.19
0.07	1.65 ± 0.20	1.23 ± 0.19	1.18 ± 0.21	1.45 ± 0.14	1.60 ± 0.16	1.49 ± 0.15	1.51 ± 0.16
0.09	0.74 ± 0.14	1.19 ± 0.19	1.27 ± 0.20	1.21 ± 0.14	1.47 ± 0.16	1.87 ± 0.17	1.09 ± 0.14
0.11	1.06 ± 0.18	0.90 ± 0.16	0.98 ± 0.17	1.13 ± 0.14	1.21 ± 0.15	1.52 ± 0.16	1.23 ± 0.16
0.13	0.85 ± 0.18	0.85 ± 0.16	0.98 ± 0.17	1.14 ± 0.14	1.24 ± 0.16	1.09 ± 0.14	1.16 ± 0.16
0.15	0.79 ± 0.18	0.73 ± 0.16	0.77 ± 0.15	0.87 ± 0.14	1.17 ± 0.17	0.93 ± 0.14	1.03 ± 0.15
0.17	0.41 ± 0.15	0.65 ± 0.16	0.84 ± 0.16	0.62 ± 0.13	0.87 ± 0.15	0.91 ± 0.15	0.90 ± 0.15
0.19	0.90 ± 0.28	0.97 ± 0.22	0.55 ± 0.14	0.85 ± 0.15	0.78 ± 0.17	0.97 ± 0.16	1.07 ± 0.17
0.21	0.17 ± 0.12	0.82 ± 0.23	0.72 ± 0.17	0.48 ± 0.14	0.73 ± 0.19	0.83 ± 0.16	1.00 ± 0.17
0.23	0.85 ± 0.40	0.48 ± 0.17	0.52 ± 0.16	0.59 ± 0.17	0.45 ± 0.16	0.53 ± 0.14	0.81 ± 0.16
0.25	0.20 ± 0.20	0.45 ± 0.20	0.38 ± 0.14	0.21 ± 0.11	0.24 ± 0.14	0.40 ± 0.14	0.65 ± 0.16
0.27		0.44 ± 0.32	0.44 ± 0.16	0.36 ± 0.16	0.17 ± 0.18	0.66 ± 0.20	0.27 ± 0.10
0.29			0.33 ± 0.20	0.49 ± 0.21	0.26 ± 0.26	0.69 ± 0.23	0.49 ± 0.16
0.31			0.19 ± 0.12	0.42 ± 0.19		0.26 ± 0.15	0.62 ± 0.18
0.33			0.18 ± 0.13	0.26 ± 0.15		0.33 ± 0.14	0.40 ± 0.17
0.35				0.45 ± 0.23		0.57 ± 0.41	0.80 ± 0.26
0.37				0.48 ± 0.24			0.41 ± 0.24
0.39				0.13 ± 0.13			0.23 ± 0.23
$\left.\frac{d\sigma}{dt}\right\|_0$ $(\frac{\mu b}{GeV^2})$	1.96 ± 0.26	1.74 ± 0.19	1.86 ± 0.17	2.23 ± 0.13	2.42 ± 0.16	2.44 ± 0.15	2.52 ± 0.13
Slope (GeV^{-2})	7.76 ± 1.27	5.13 ± 0.96	5.79 ± 0.68	6.45 ± 0.54	6.36 ± 0.63	5.76 ± 0.52	5.88 ± 0.44

TABLE 4

Experiment	Photon Energy (GeV)	S (GeV^2)	Slope ($|t| < 0.4$) (GeV^{-2})
Bonn	2	4.64	4.55 ± 0.85
S.B.T.	2.8 + 4.7	8.4	5.67 ± 1.83
C-72	8.5	16.9	6.55 ± 0.58
S-W	9.3	18.4	4.16 ± 1.56
S-CT	12	23.4	5.49 ± 1.20
	13	25.3	6.83 ± 2.29
	14	27.1	6.22 ± 2.47

TABLE 5

Experiment	Photon Energy (GeV)	S (GeV^2)	Slope at $\|t\| = 0.2$ GeV^2 (GeV^{-2})
D-K	3.0 - 5.6	9.0	5.81 ± 0.20
S-B-T	2.8 - 4.7		
D-BC	2.5 - 5.8		
D-MIT	5.2		
D-K	5.6 - 6.7	12.6	5.22 ± 0.19
S-CT	6.0 - 6.5		
S-B-T	9.3	17.6	5.86 ± 0.24
C-72	8.5		
S-W	9.0		

Table 6 a

Helicity System

Photon Energy (GeV)	4.65 - 5.68			5.68 - 6.71		
$\lvert t-t_{min}\rvert$ (GeV^2)	ρ_{00}	Re ρ_{10}	ρ_{1-1}	ρ_{00}	Re ρ_{10}	ρ_{1-1}
0.00 - 0.04	-0.05 ± 0.03	-0.04 ± 0.03	-0.03 ± 0.04	-0.02 ± 0.03	-0.01 ± 0.03	-0.07 ± 0.04
0.04 - 0.08	0.00 ± 0.03	-0.05 ± 0.03	-0.10 ± 0.05	0.00 ± 0.03	-0.03 ± 0.03	-0.08 ± 0.05
0.08 - 0.12	0.03 ± 0.06	-0.05 ± 0.04	0.10 ± 0.07	0.02 ± 0.04	-0.07 ± 0.03	0.00 ± 0.06
0.12 - 0.16	0.00 ± 0.06	0.00 ± 0.04	0.04 ± 0.08	-0.01 ± 0.05	-0.08 ± 0.05	-0.03 ± 0.07
0.16 - 0.20	0.07 ± 0.10	-0.03 ± 0.07	-0.02 ± 0.11	-0.02 ± 0.03	-0.07 ± 0.03	0.10 ± 0.09
0.20 - 0.24				0.04 ± 0.08	0.01 ± 0.06	-0.11 ± 0.09

Table 6 b

Gottfried-Jackson System

Photon Energy (GeV)	4.64 - 5.68			5.68 - 6.71		
$\lvert t-t_{min}\rvert$ (GeV^2)	ρ_{00}	Re ρ_{10}	ρ_{1-1}	ρ_{00}	Re ρ_{10}	ρ_{1-1}
0.00 - 0.04	-0.03 ± 0.04	0.08 ± 0.03	-0.02 ± 0.04	0.02 ± 0.04	0.11 ± 0.03	-0.05 ± 0.04
0.04 - 0.08	0.09 ± 0.05	0.16 ± 0.03	-0.05 ± 0.05	0.11 ± 0.05	0.16 ± 0.03	-0.03 ± 0.05
0.08 - 0.12	0.11 ± 0.05	0.11 ± 0.04	0.14 ± 0.06	0.11 ± 0.05	0.15 ± 0.04	0.04 ± 0.06
0.12 - 0.16	0.24 ± 0.08	0.16 ± 0.05	0.16 ± 0.07	0.15 ± 0.08	0.19 ± 0.05	0.05 ± 0.07
0.16 - 0.20	0.29 ± 0.07	0.15 ± 0.04	0.09 ± 0.07	0.14 ± 0.07	0.16 ± 0.04	0.18 ± 0.07
0.20 - 0.24				0.42 ± 0.10	0.18 ± 0.07	0.08 ± 0.08

Table 7

Fit condition	$\alpha'(0)$	$r_{11_{1/2-1/2}}$	$r_{01_{1/2\ 1/2}}$	$r_{11_{1/2\ 1/2}}$	χ^2/DF
A	0.22	0.10 ± 0.66	2.26 ± 0.15	-30.90 ± 10.41	12.2/14
B	0.27	0.01 ± 0.17	2.23 ± 0.15	-25.36 ± 8.39	12.2/14
C	0.23 ± 0.50	0.05 ± 0.54	2.25 ± 0.17	-30.83 ± 75.68	12.2/13

Fit condition	g	a	b	χ^2/DF	t-dependence
D	8.58 ± 0.09	1.43 ± 0.09	0.58 ± 0.11	171.8/78	$e^{-(a\|t\| + bt^2)}$
E	8.91 ± 0.07	1.90 ± 0.03	0	203.8/79	$e^{-a\|t\|}$

Table 8

$t-t_{min}$ (GeV^2)	Incident photon energy (GeV)			
	4.5 - 5.1	5.1 - 5.6	5.6 - 6.2	6.2 - 6.7
0.01	0.89 ± 0.09	0.94 ± 0.09	1.00 ± 0.10	0.66 ± 0.06
0.03	0.89 ± 0.09	0.96 ± 0.09	0.96 ± 0.09	0.66 ± 0.06
0.05	0.69 ± 0.07	0.95 ± 0.09	0.92 ± 0.09	0.50 ± 0.05
0.07	0.80 ± 0.08	0.91 ± 0.09	0.94 ± 0.09	0.57 ± 0.05
0.09	0.79 ± 0.08	0.88 ± 0.09	0.78 ± 0.08	0.52 ± 0.05
0.11	0.68 ± 0.07	0.93 ± 0.09	0.62 ± 0.06	0.50 ± 0.05
0.13	0.72 ± 0.07	0.80 ± 0.08	0.59 ± 0.06	0.51 ± 0.05
0.15	0.93 ± 0.09	0.59 ± 0.06	0.47 ± 0.05	0.48 ± 0.05
0.17	0.68 ± 0.07	1.03 ± 0.10	0.60 ± 0.06	0.45 ± 0.04
$\left.\frac{d\sigma}{dt}\right\|_{t=t_{min}} \left(\frac{\mu b}{GeV^2}\right)$	0.87 ± 0.07	0.98 ± 0.06	1.1 ± 0.07	0.66 ± 0.10
$B(GeV^{-2})$	1.47 ± 0.80	1.44 ± 0.70	4.36 ± 0.50	2.29 ± 0.50

Figure Captions

1. The production mechanism of the ϕ meson based on the vector meson dominance model. The elastic ϕ is produced by the exchange of a single pomeron trajectory.

2. The experimental set up used for Exp I.

3. The distribution of photons observed in the tagging channel. The solid curve represents an expected spectrum from the bremsstrahlung process.

4. Schematic drawings of the Cerenkov counter, (a) side view and (b) top view. The Cerenkov light is reflected and focussed by six mirrors into phototubes.

5. The horizontal, vertical and longitudinal projections of the reconstructed vertices are compared with the target boundaries and the vacuum windows.

6. The event distribution for invariant K^+K^- mass versus recoil mass.

7. The invariant K^+K^- mass distribution for recoil masses in the proton region.

8. Probability distribution for a 1-C kinematic fit.

9. The invariant $\pi^+\pi^-$ mass of events when both particle momenta were below the Cerenkov - threshold and the vertex downstream of the target.

10. The t-dependence of the differential cross section for the elastic process at different photon energies. The straight lines are fits to a linear exponential form.

11. The energy dependence of the optical point. The curve is the best fit to the data of this experiment.

12. Relation between σ_{tot} and $\gamma_\phi^2/4\pi$ due to equation (2.4) represented by $C = (1.14 \pm 0.03) \cdot 10^{-3}$ mb^2 as determined in this experiment.

13. A fit of B of the relation (2.8) as a function of s in the region $|t| \leq 0.4$ GeV^2.

14. The slope value B at $|t| = 0.2$ GeV^2 plotted as a function of s. The black points are obtained from photoproduction data and the open circles are from ref. 15. The solid curve represents an effective slope from "$\phi p \to \phi p$": 0.19 ± 0.02 GeV^2.

15. Definition of decay angles in the helicity and Gottfried-Jackson system.

16. t-dependence of the ϕ spin density matrix elements evaluated for two energy regions
a) in the helicity frame
b) in the Gottfried-Jackson frame.

17. K^+K^- decay angular distributions in the helicity frame as a function of the invariant K^+K^- mass. Solid lines are fits of a superposition of Legendre polynomials to the data.

18. Spin density matrix elements computed from the diffractive helicity amplitudes (§6) together with experimental results
a) in the helicity frame and
b) in the Gottfried-Jackson system.

19. The elastic differential cross sections are plotted as a function of t together with other experimental results. The curves obtained on the basis of the helicity amplitude analysis (§6) are drawn for the assumptions D (dashed line ---) and E (longer dash —). A linear exponential fit to the data in the region $t > 0.4$ GeV^2, yielding an intercept of 1.44 ± 0.16 GeV^2 and a slope of $B = 4.05 \pm 0.19$ GeV^{-2} are drawn as a solid line.

20. The t dependence of the helicity amplitudes computed for diffractive ϕ photoproduction are drawn as solid lines. For comparison, the helicity amplitudes for the ρ^o photoproduction are shown by the dashed curves.

21. Real to imaginary ratio of the (SHC) amplitude as computed in §6.

22. Normalized moments of spherical harmonics of the K^+K^- decay distribution in the helicity system as a function of the K^+K^- invariant mass.

23. Invariant K^+K^- mass for $1.2 \leq M_X \leq 2.1$ GeV in the reaction $\gamma p \to K^+K^-X$ for two experimental cuts a) and b).

24. The double inelastic cross sections $d^2\sigma/dM_X d(t-t_{min})$ as a function of $t-t_{min}$ for different regions in M_X.

25. The inelastic cross section with respect to momentum transfer $t-t_{min}$ for 4 different energy regions.

26. Slope of the $t-t_{min}$ - distribution of the double differential cross section as a function of M_X together with results from the reaction $K^+p \to K^+X$.

27. The ratio of inelastic to elastic differential cross sections at $t=t_{min}$ for different γ-energies.

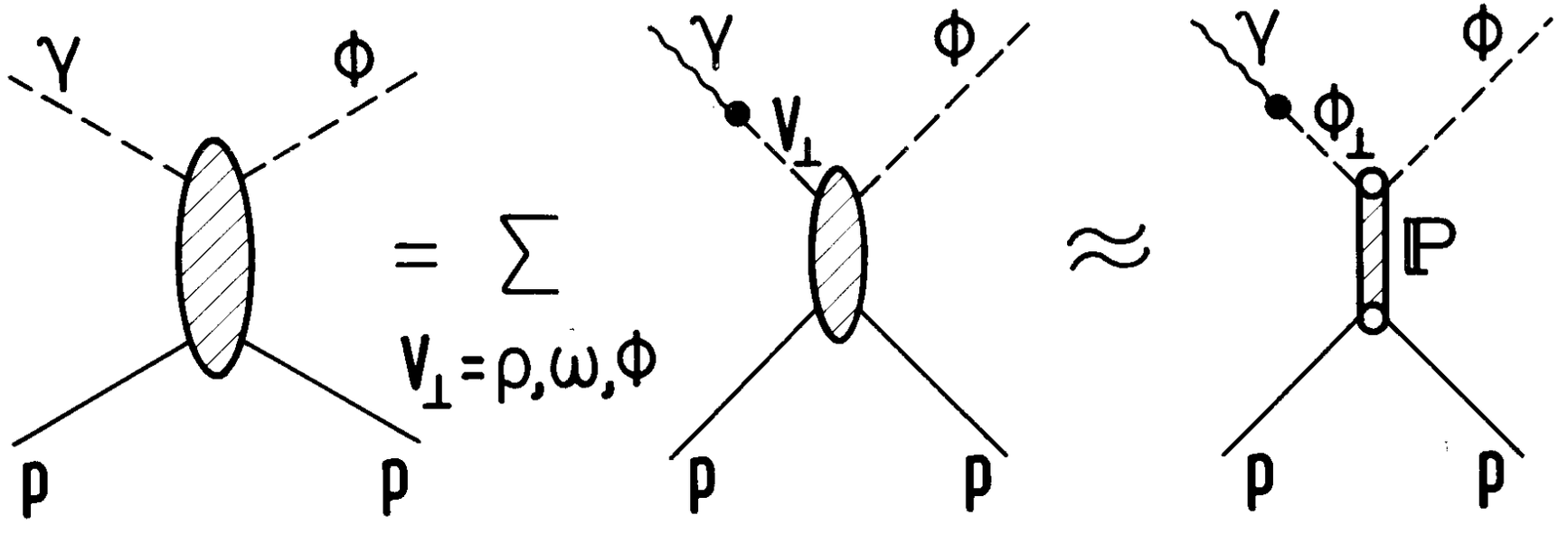

2760

FIG.1

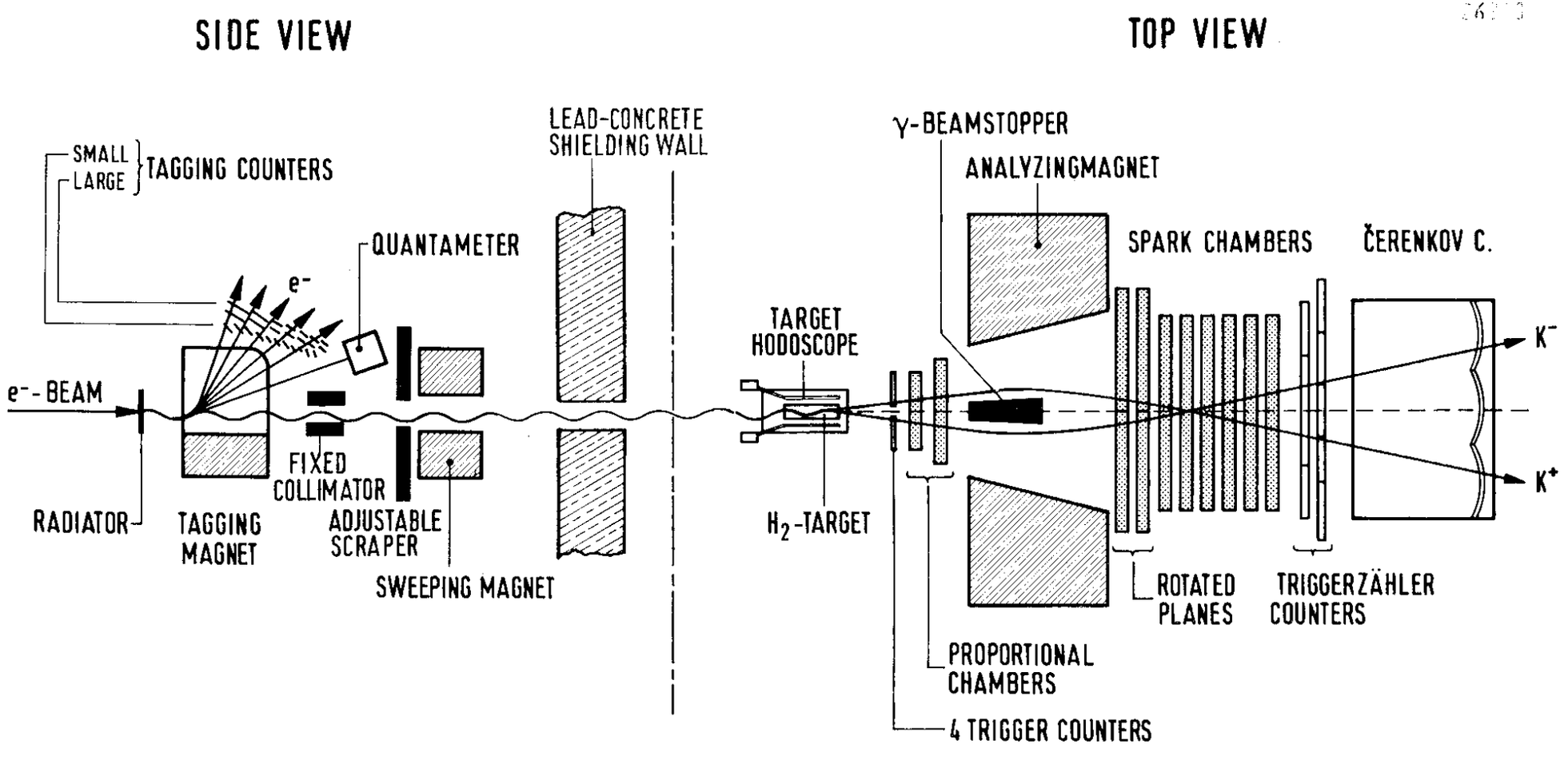
SIDE VIEW
TOP VIEW
SMALL
LARGE
TAGGING COUNTERS
QUANTAMETER
e⁻
LEAD-CONCRETE
SHIELDING WALL
γ-BEAMSTOPPER
ANALYZINGMAGNET
SPARK CHAMBERS
ČERENKOV C.
TARGET
HODOSCOPE
e⁻-BEAM
K⁻
K⁺
FIXED
COLLIMATOR
RADIATOR
TAGGING
MAGNET
ADJUSTABLE
SCRAPER
SWEEPING MAGNET
H₂-TARGET
ROTATED
PLANES
TRIGGERZÄHLER
COUNTERS
PROPORTIONAL
CHAMBERS
4 TRIGGER COUNTERS

FIG.2

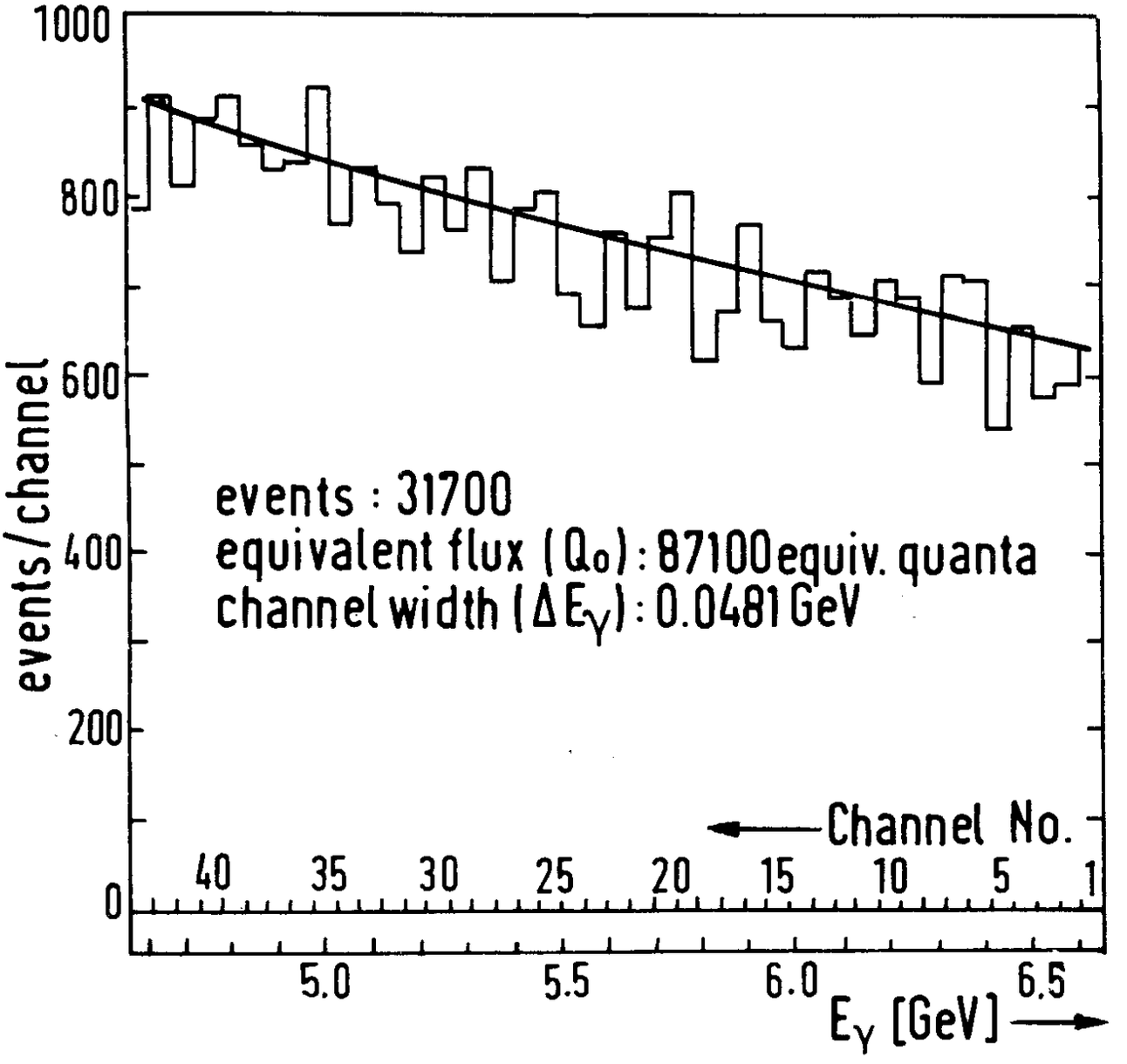
1000
800
600
400
200
0
events/channel
events : 31700
equivalent flux (Q₀) : 87100 equiv. quanta
channel width (ΔEγ) : 0.0481 GeV
Channel No.
40 35 30 25 20 15 10 5 1
5.0 5.5 6.0 6.5
Eγ [GeV]

FIG.3

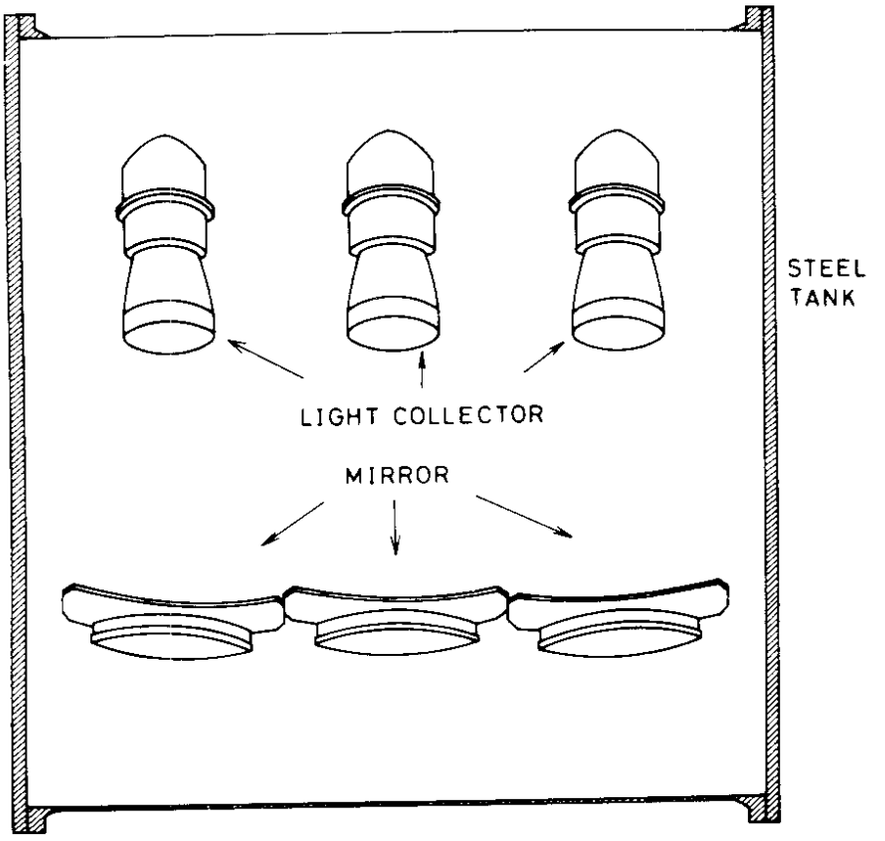
STEEL
TANK
LIGHT COLLECTOR
MIRROR

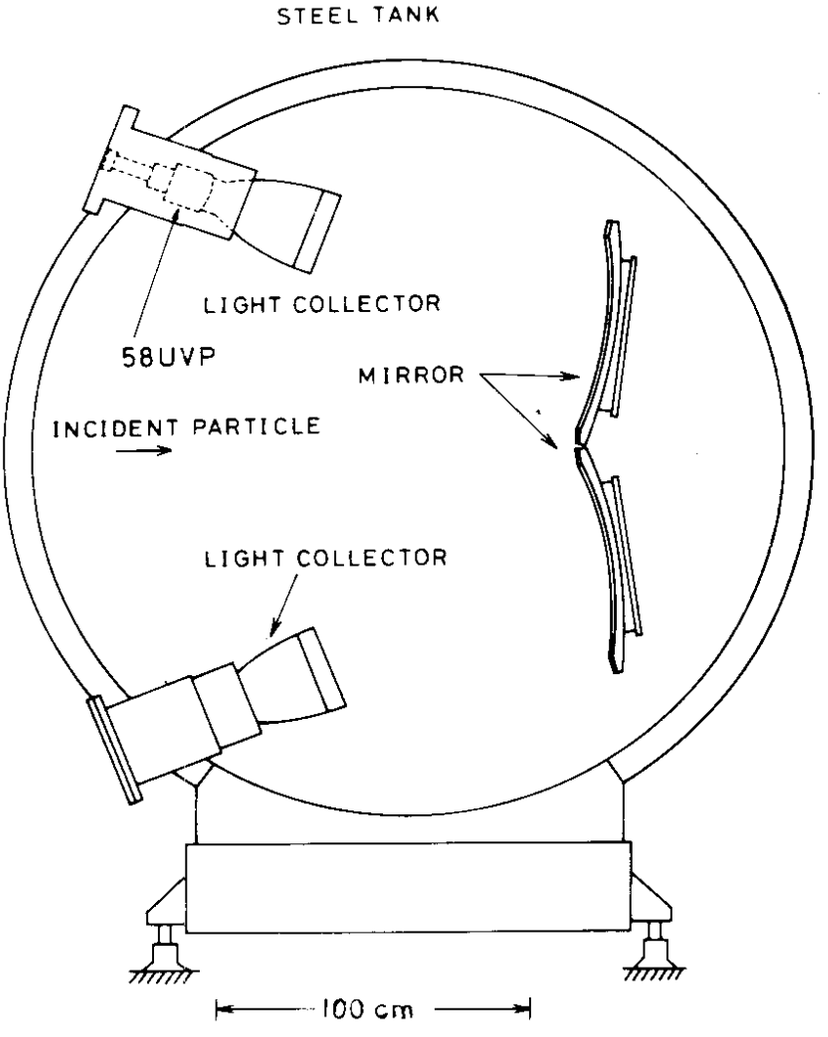
STEEL TANK
LIGHT COLLECTOR
58UVP
MIRROR
INCIDENT PARTICLE
LIGHT COLLECTOR
100 cm

FIG.4

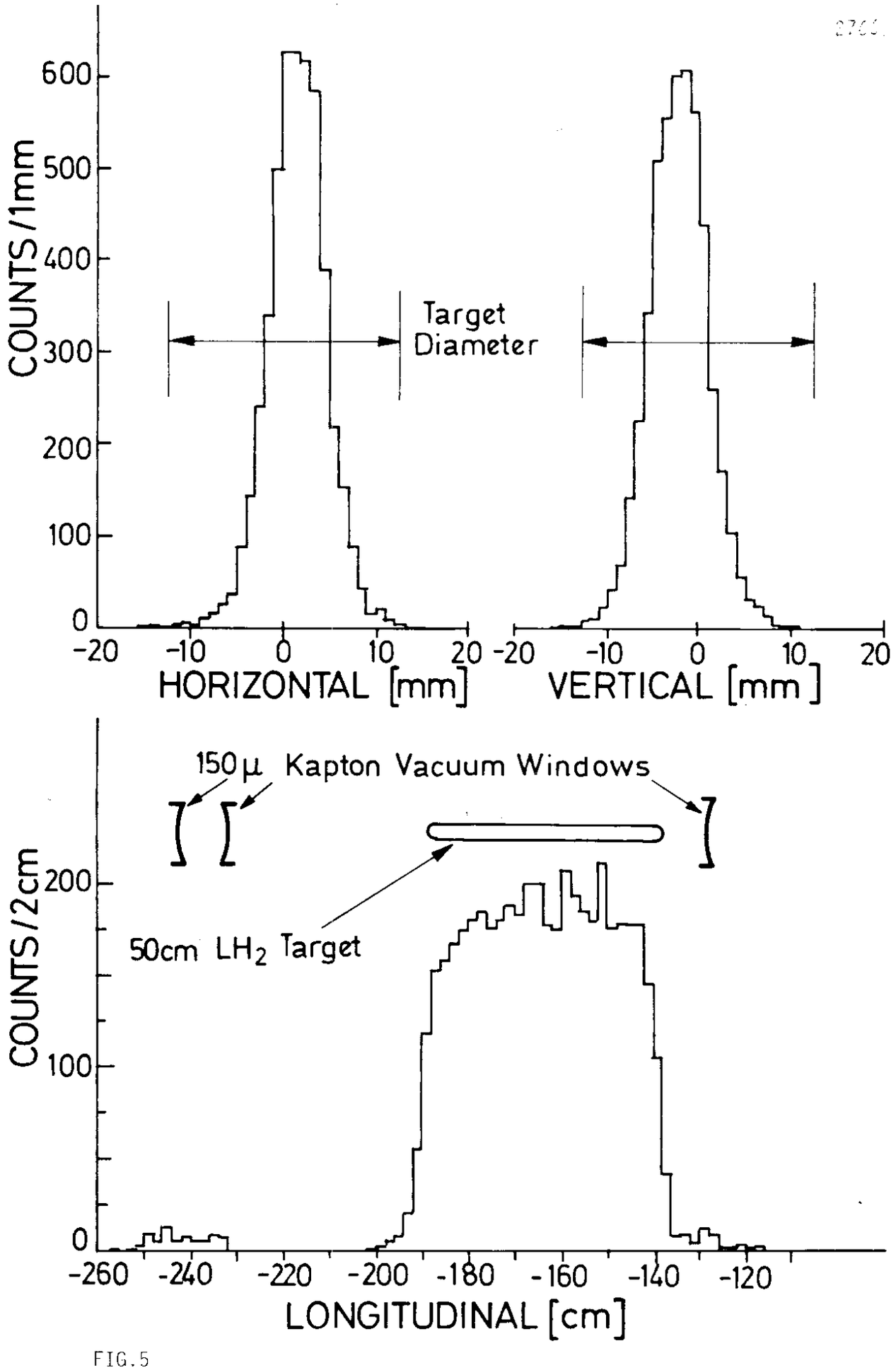
COUNTS/1mm
600
500
400
300
200
100
0
Target
Diameter
-20
-10
0
10
20
HORIZONTAL [mm]
VERTICAL [mm]
150μ Kapton Vacuum Windows
50cm LH2 Target
COUNTS/2cm
200
100
0
-260
-240
-220
-200
-180
-160
-140
-120
LONGITUDINAL [cm]

FIG.5

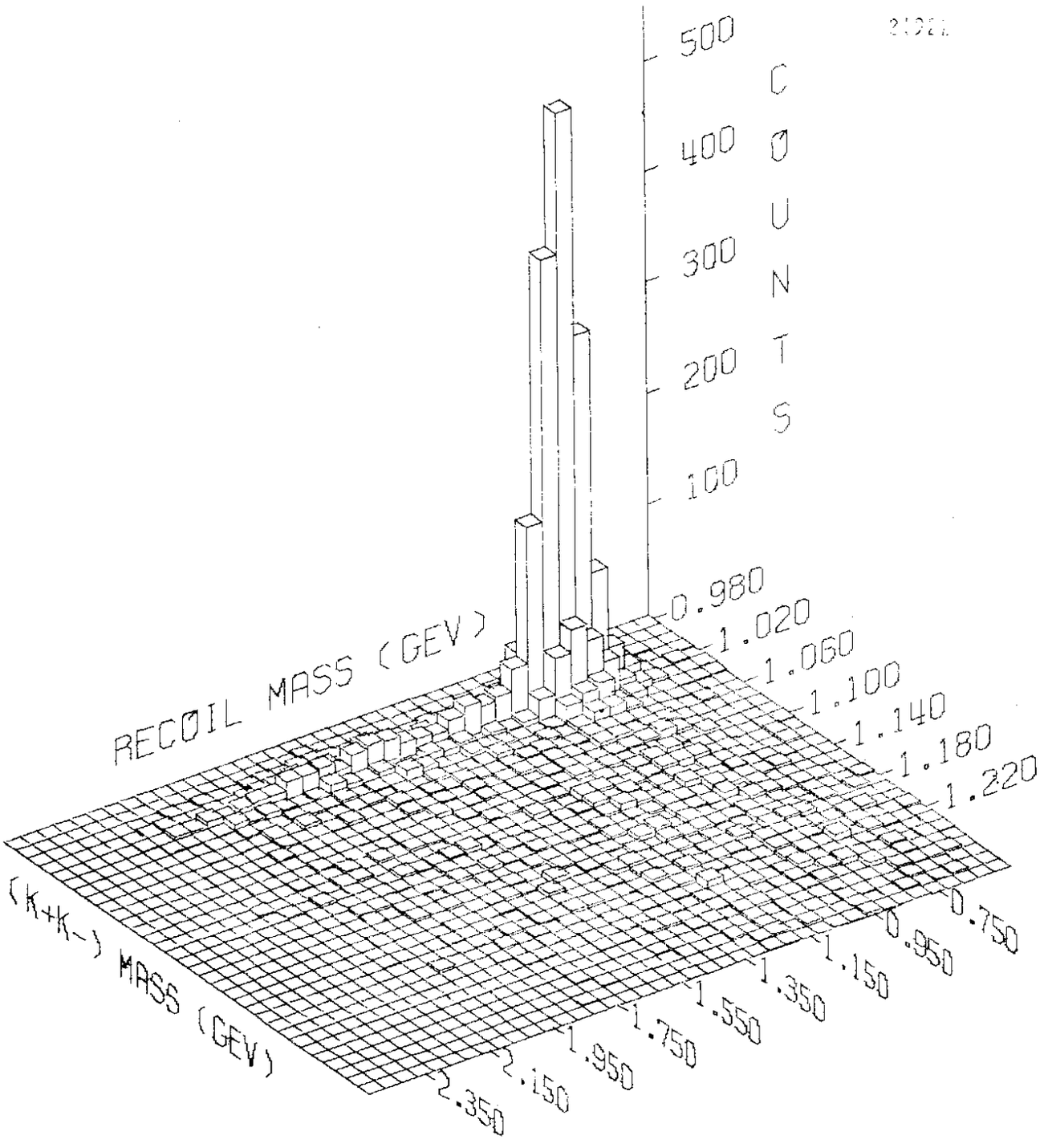
500
400
300
200
100
COUNTS
RECOIL MASS (GEV)
0.980
1.020
1.060
1.100
1.140
1.180
1.220
(K+K-) MASS (GEV)
0.750
0.950
1.150
1.350
1.550
1.750
1.950
2.150
2.350

FIG.6

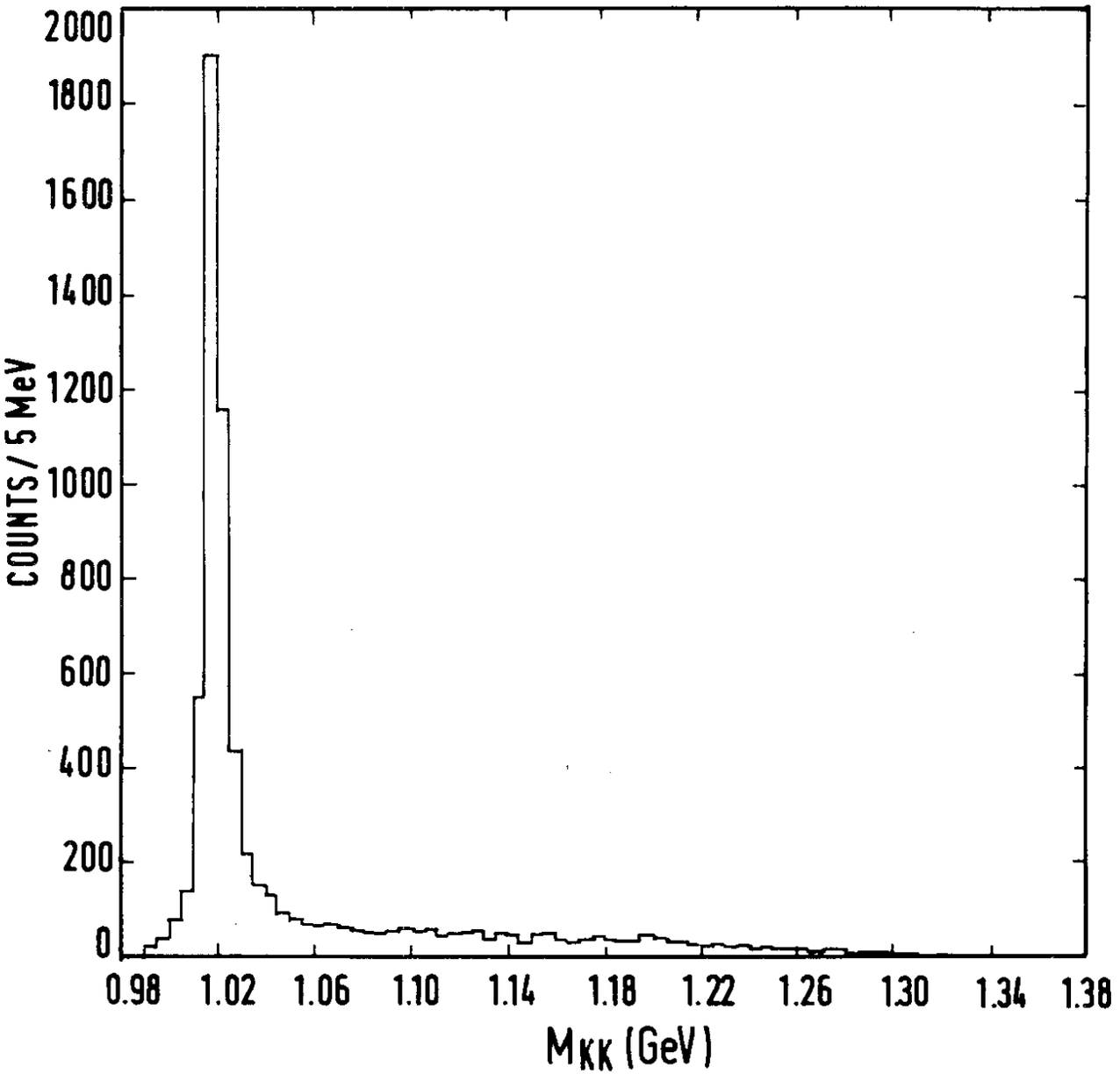
2000
1800
1600
1400
1200
1000
800
600
400
200
0
COUNTS / 5 MeV
0.98
1.02
1.06
1.10
1.14
1.18
1.22
1.26
1.30
1.34
1.38
MKK (GeV)

FIG.7

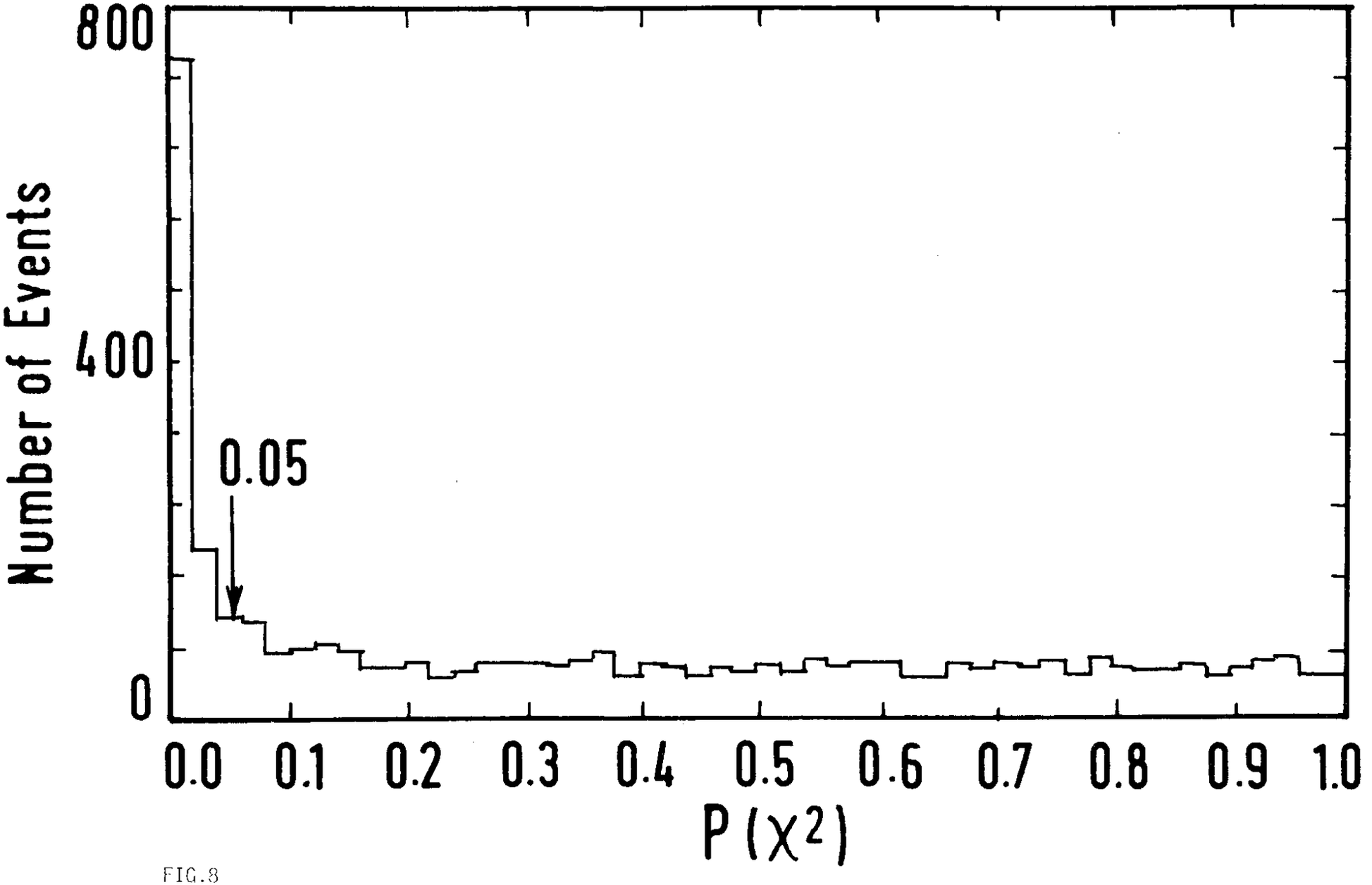

FIG.8

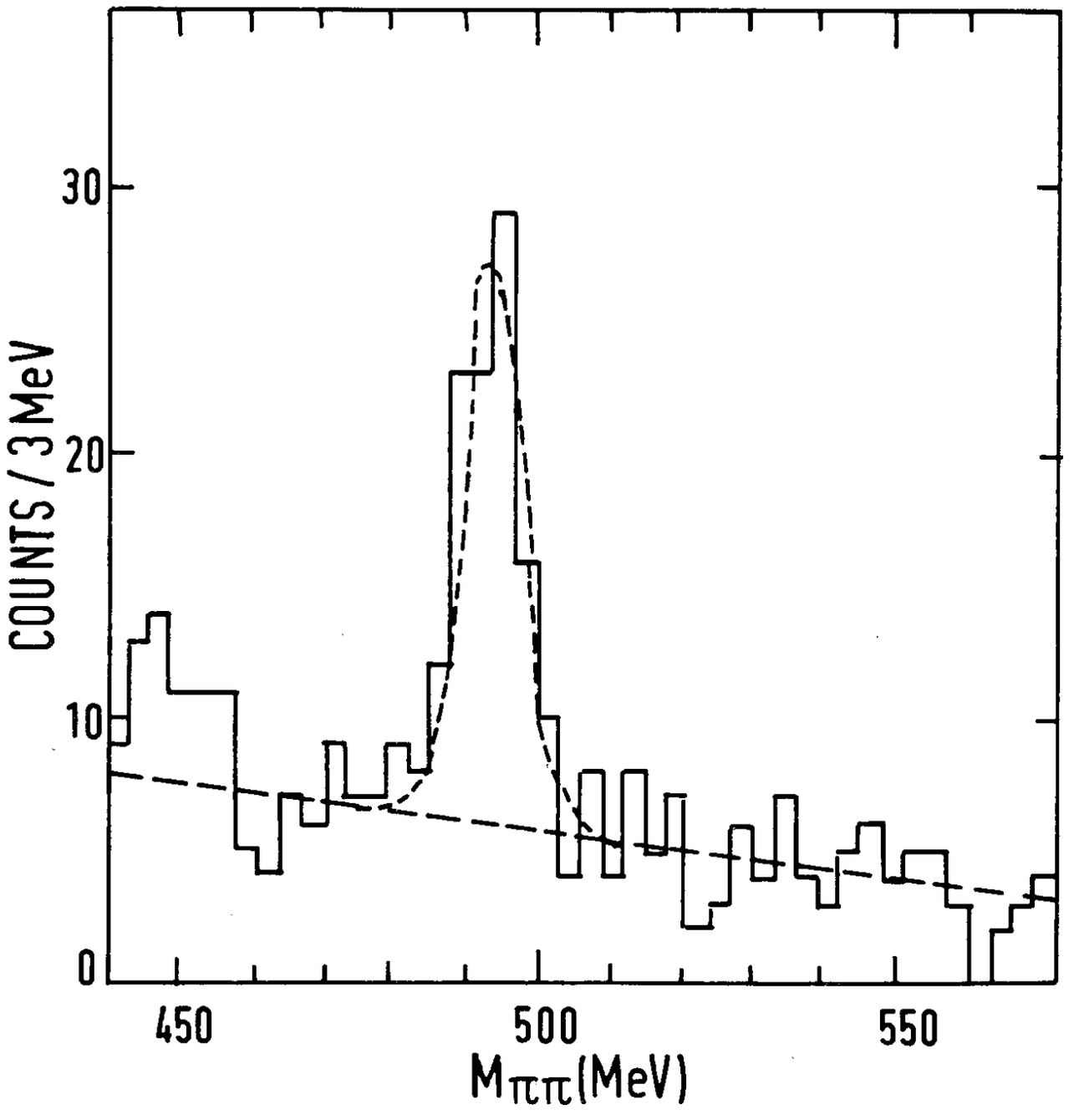

FIG.9

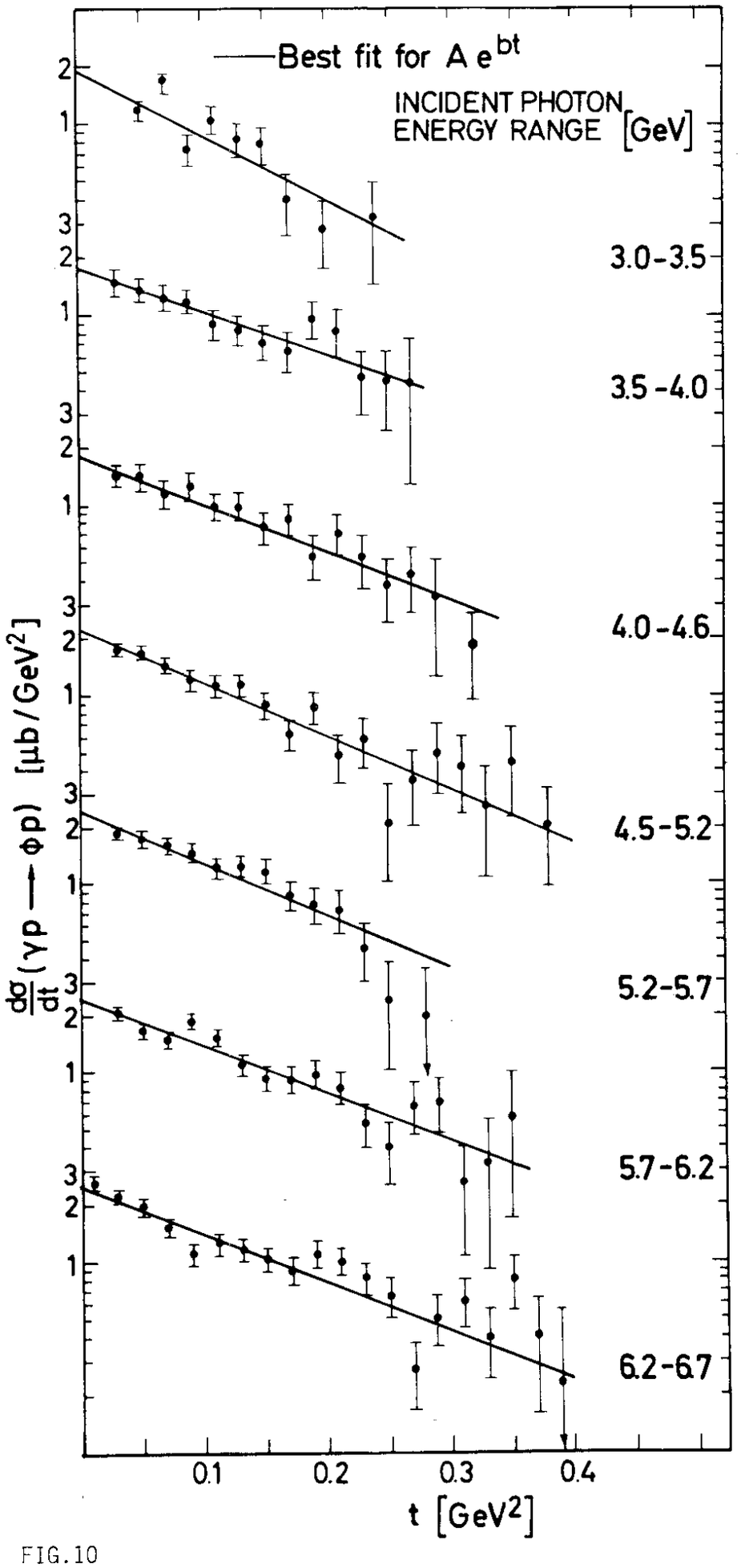
Best fit for A e^bt
INCIDENT PHOTON ENERGY RANGE [GeV]
3.0-3.5
3.5-4.0
4.0-4.6
4.5-5.2
5.2-5.7
5.7-6.2
6.2-6.7
dσ/dt (γp → φp) [μb/GeV²]
t [GeV²]
0.1
0.2
0.3
0.4

FIG.10

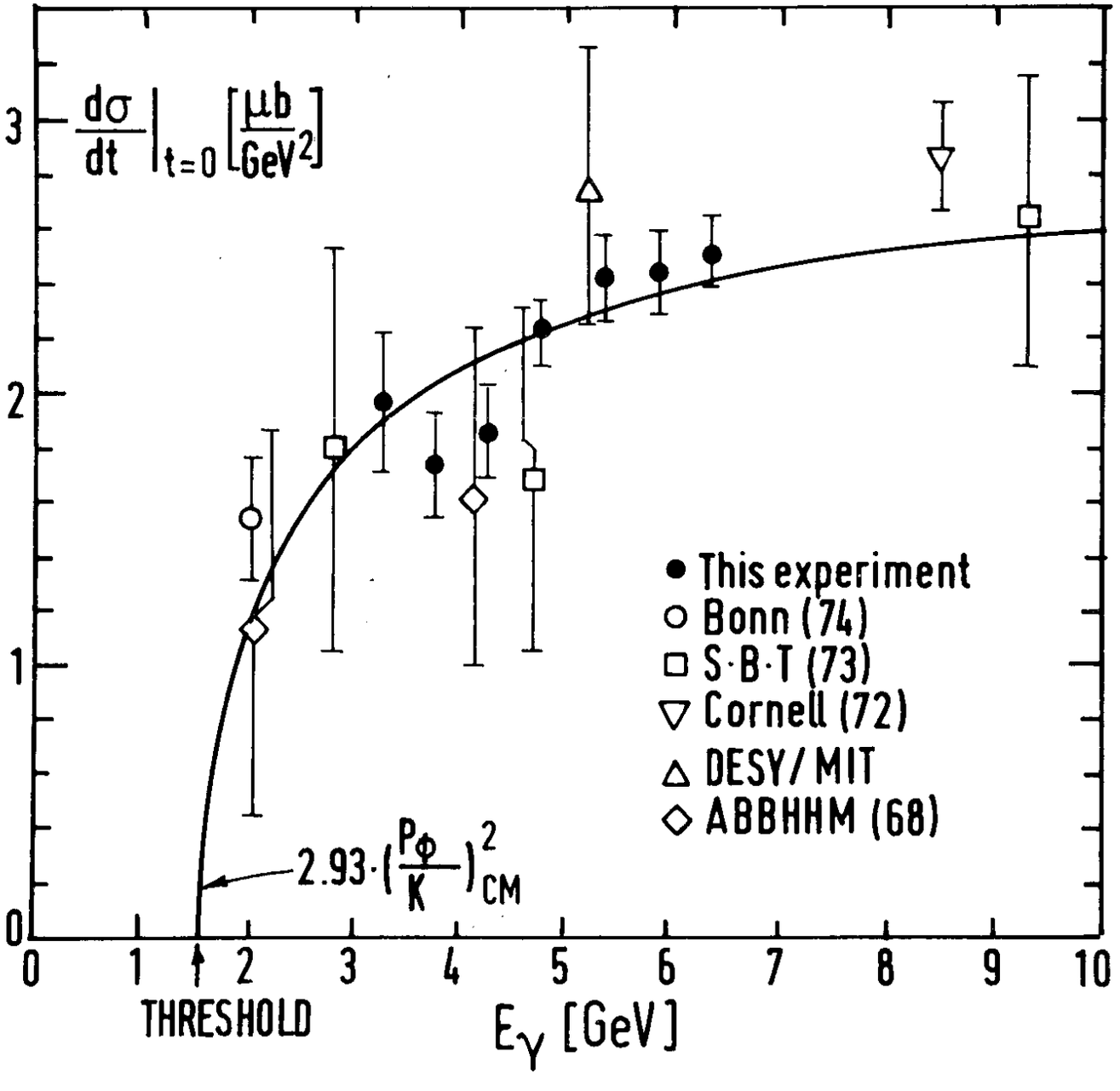
$\frac{d\sigma}{dt}\Big|_{t=0}\left[\frac{\mu b}{GeV^2}\right]$
3
2
1
0
0
1
2
3
4
5
6
7
8
9
10
THRESHOLD
E_γ [GeV]
$2.93\cdot\left(\frac{P_\phi}{K}\right)^2_{CM}$
● This experiment
○ Bonn (74)
□ S·B·T (73)
▽ Cornell (72)
△ DESY/MIT
◇ ABBHHM (68)

FIG.11

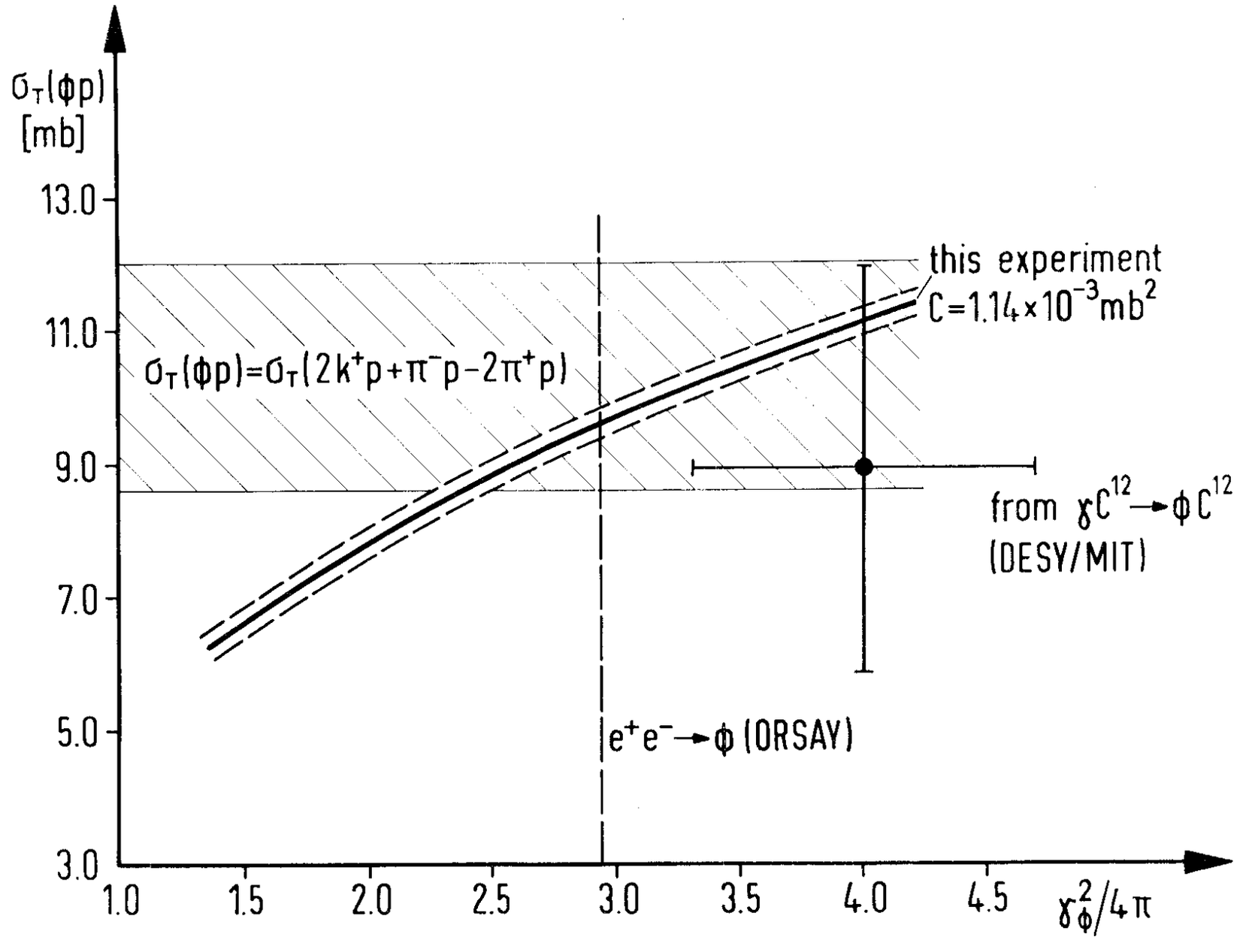
$\sigma_T(\phi p)$ [mb]
13.0
11.0
9.0
7.0
5.0
3.0
1.0
1.5
2.0
2.5
3.0
3.5
4.0
4.5
$\gamma^2_\phi/4\pi$
$\sigma_T(\phi p)=\sigma_T(2k^+p+\pi^-p-2\pi^+p)$
this experiment
$C=1.14\times10^{-3}mb^2$
from $\gamma C^{12}\rightarrow\phi C^{12}$
(DESY/MIT)
$e^+e^-\rightarrow\phi$ (ORSAY)

FIG.12

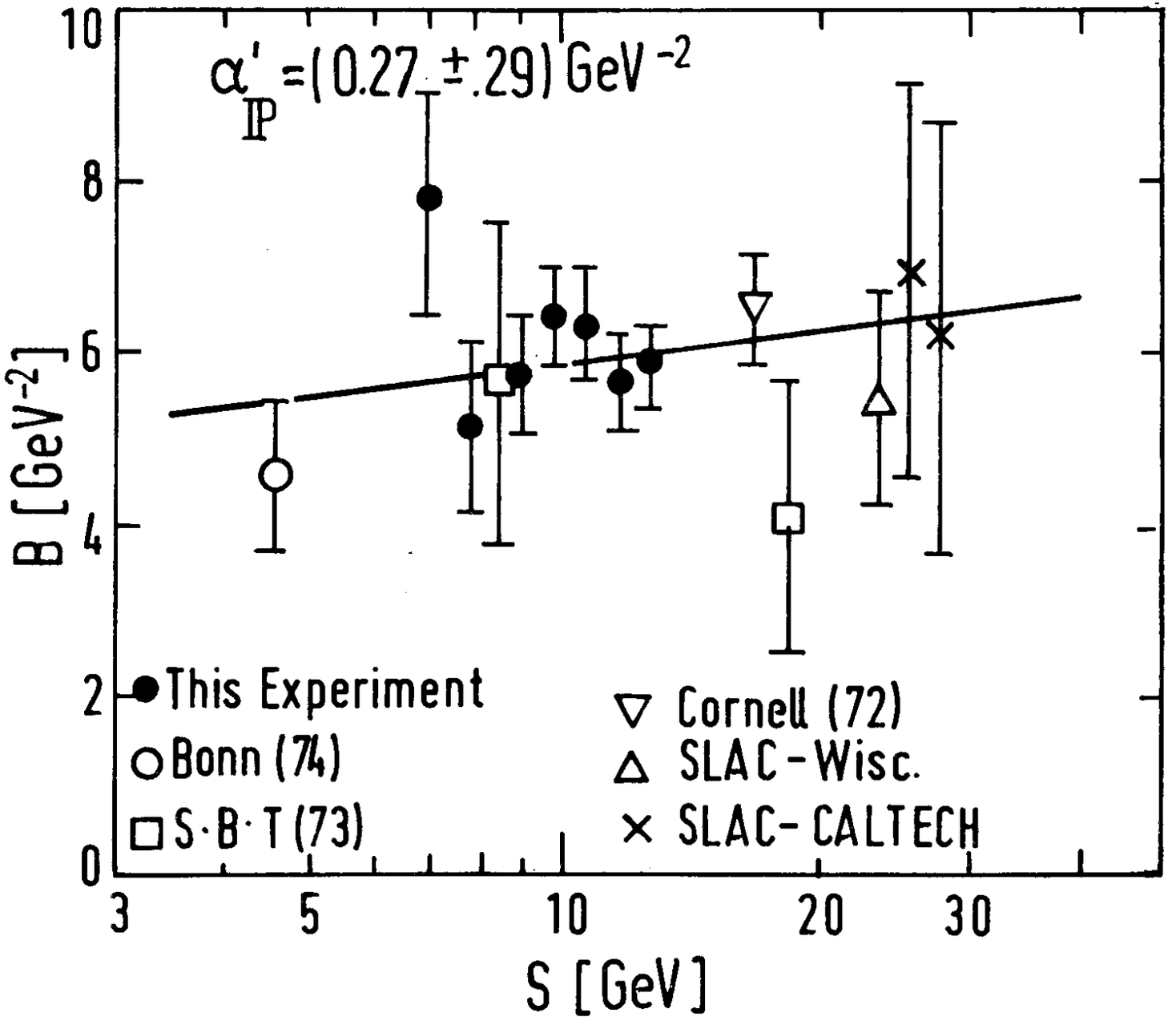
$\alpha'_{IP} = (0.27 \pm .29)\ GeV^{-2}$
B [GeV^{-2}]
S [GeV]
10
8
6
4
2
0
3
5
10
20
30
This Experiment
Bonn (74)
S·B·T (73)
Cornell (72)
SLAC-Wisc.
SLAC-CALTECH

FIG.13

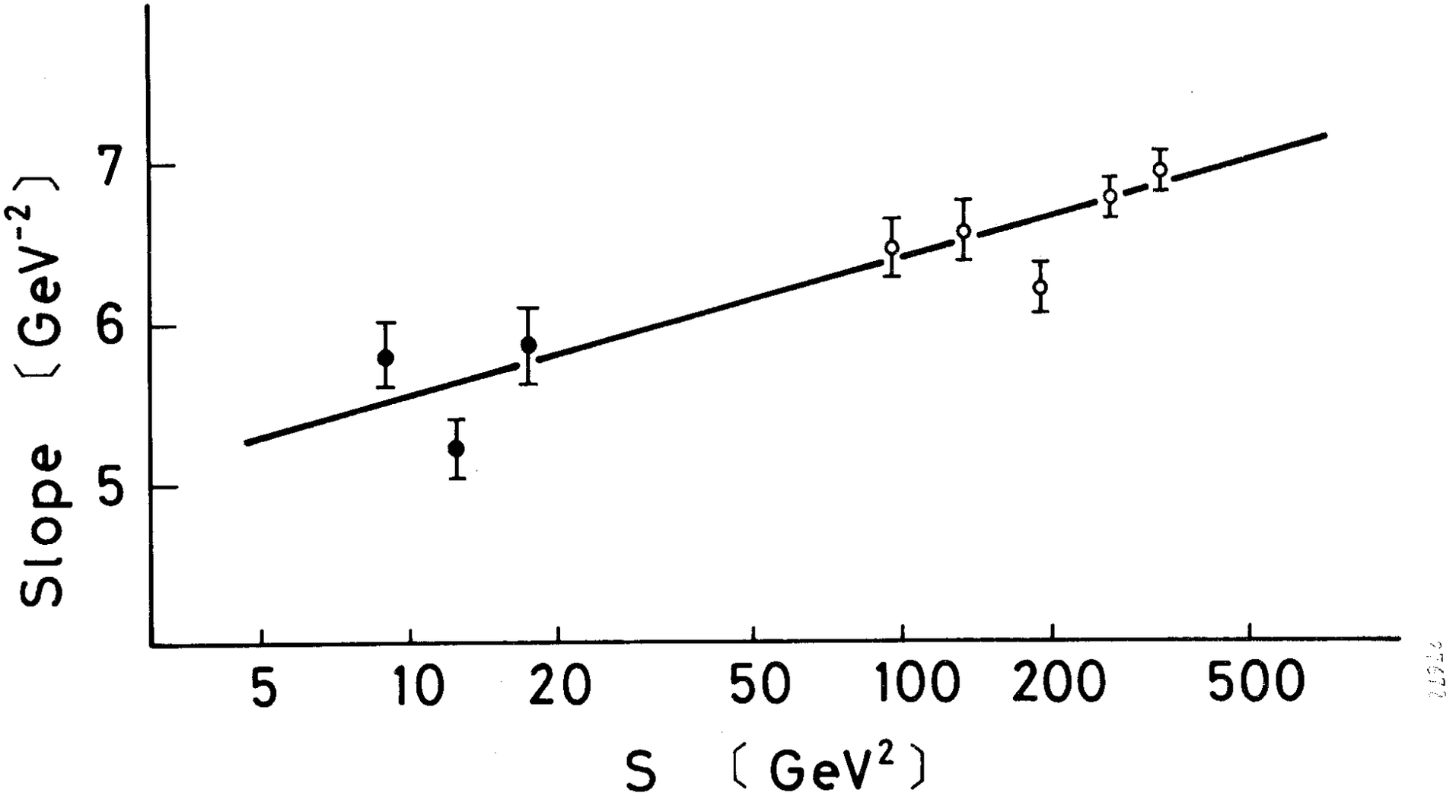

FIG.14

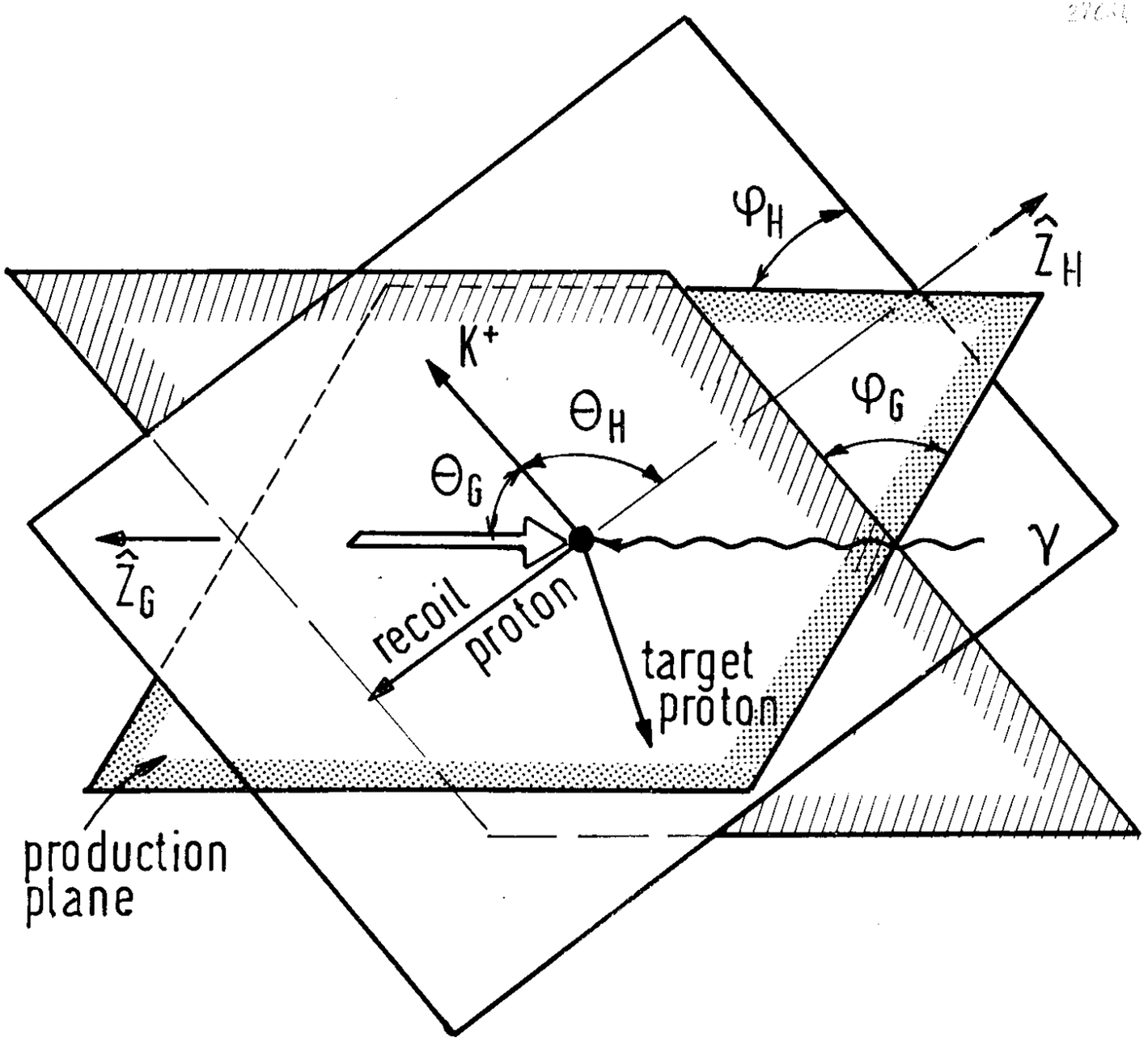
φ_H
$\hat{Z}_H$
K^+
φ_G
Θ_H
Θ_G
γ
$\hat{Z}_G$
recoil proton
target proton
production plane

FIG.15

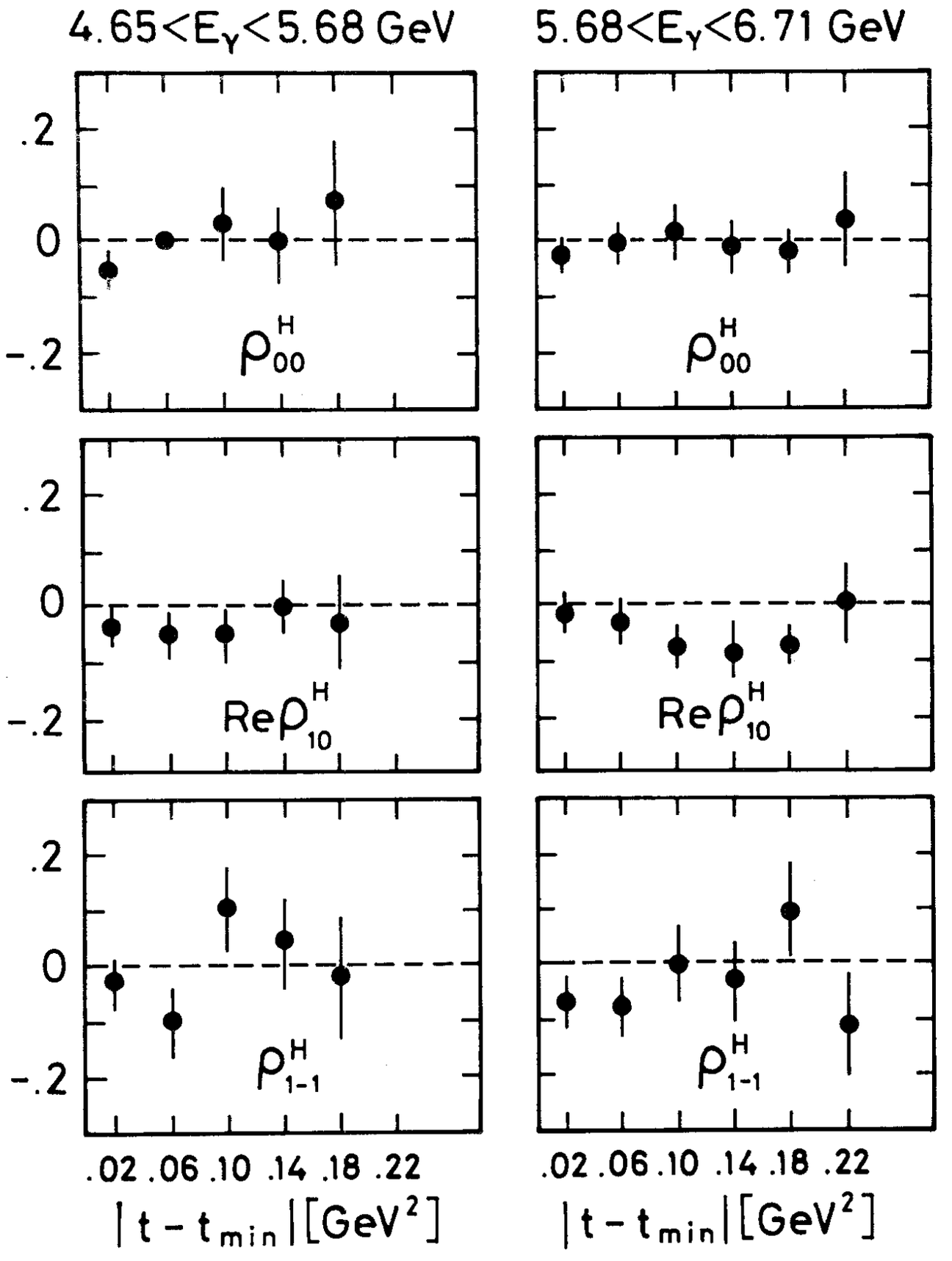
4.65<E$_\gamma$<5.68 GeV
5.68<E$_\gamma$<6.71 GeV
.2
0
-.2
ρ^H_{00}
Reρ^H_{10}
ρ^H_{1-1}
.02 .06 .10 .14 .18 .22
$|t-t_{min}|$[GeV^2]

FIG.16a

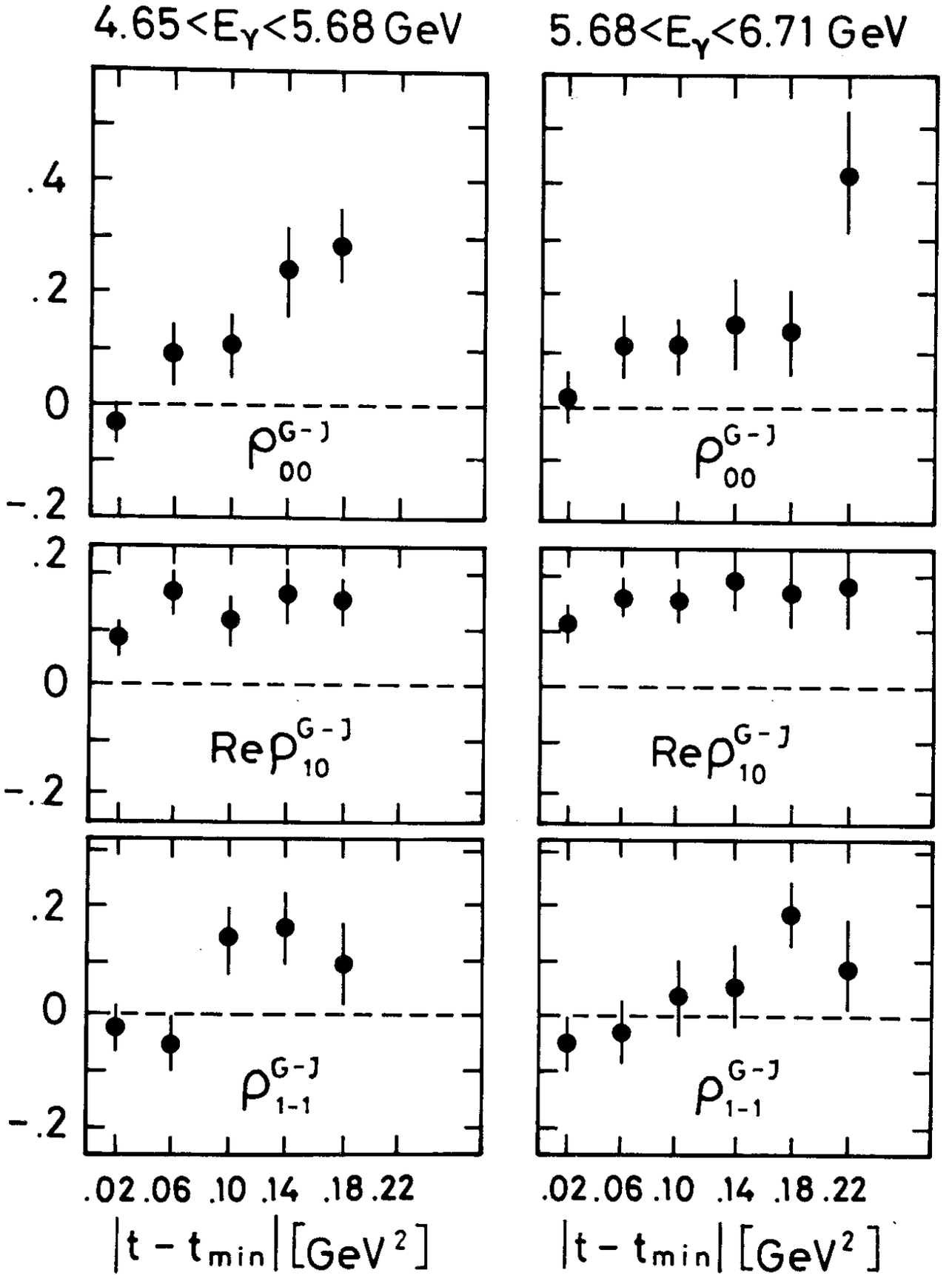
4.65<E$_\gamma$<5.68 GeV
5.68<E$_\gamma$<6.71 GeV
.4
.2
0
-.2
ρ^{G-J}_{00}
Reρ^{G-J}_{10}
ρ^{G-J}_{1-1}
.02 .06 .10 .14 .18 .22
$|t - t_{min}|$ [GeV^2]

FIG.16b

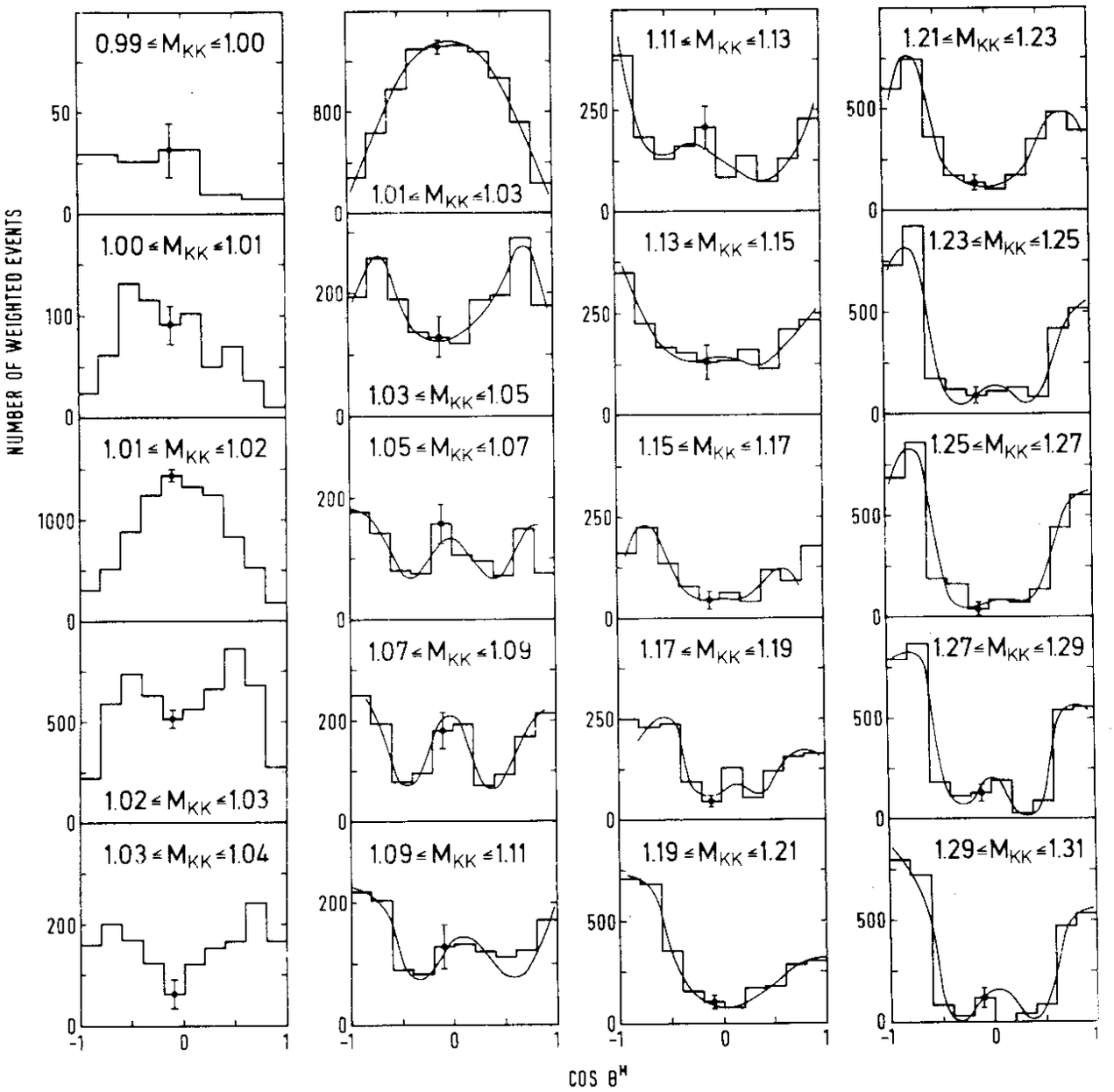
0.99 ≤ M_KK ≤ 1.00
1.00 ≤ M_KK ≤ 1.01
1.01 ≤ M_KK ≤ 1.02
1.02 ≤ M_KK ≤ 1.03
1.03 ≤ M_KK ≤ 1.04
1.01 ≤ M_KK ≤ 1.03
1.03 ≤ M_KK ≤ 1.05
1.05 ≤ M_KK ≤ 1.07
1.07 ≤ M_KK ≤ 1.09
1.09 ≤ M_KK ≤ 1.11
1.11 ≤ M_KK ≤ 1.13
1.13 ≤ M_KK ≤ 1.15
1.15 ≤ M_KK ≤ 1.17
1.17 ≤ M_KK ≤ 1.19
1.19 ≤ M_KK ≤ 1.21
1.21 ≤ M_KK ≤ 1.23
1.23 ≤ M_KK ≤ 1.25
1.25 ≤ M_KK ≤ 1.27
1.27 ≤ M_KK ≤ 1.29
1.29 ≤ M_KK ≤ 1.31
NUMBER OF WEIGHTED EVENTS
COS θ^H

FIG.17

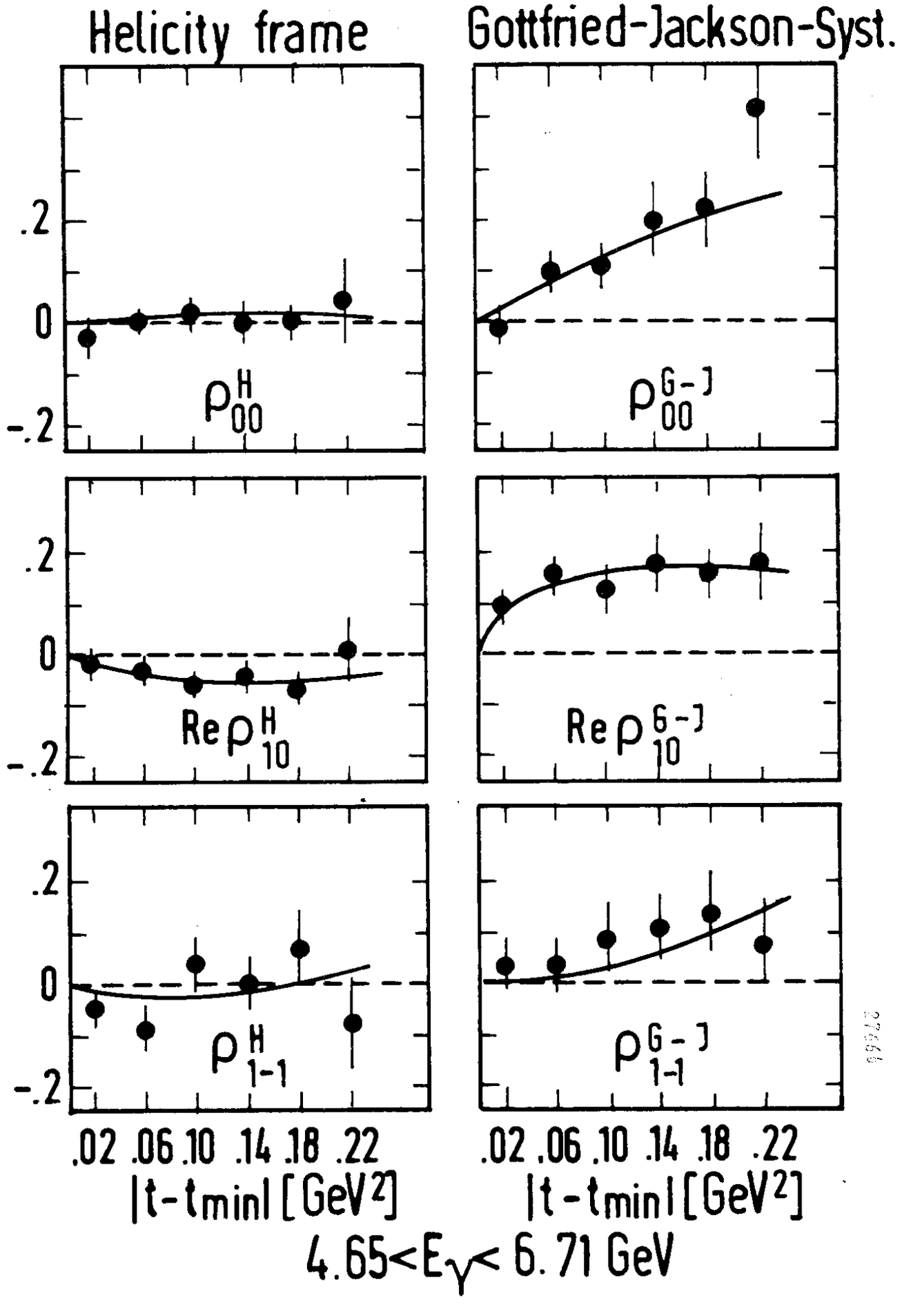
Helicity frame
Gottfried-Jackson-Syst.
.2
0
-.2
ρ^H_{00}
ρ^{G-J}_{00}
$\mathrm{Re}\,\rho^H_{10}$
$\mathrm{Re}\,\rho^{G-J}_{10}$
ρ^H_{1-1}
ρ^{G-J}_{1-1}
.02 .06 .10 .14 .18 .22
|t-tmin| [GeV²]
4.65<Eγ< 6.71 GeV

FIG.18

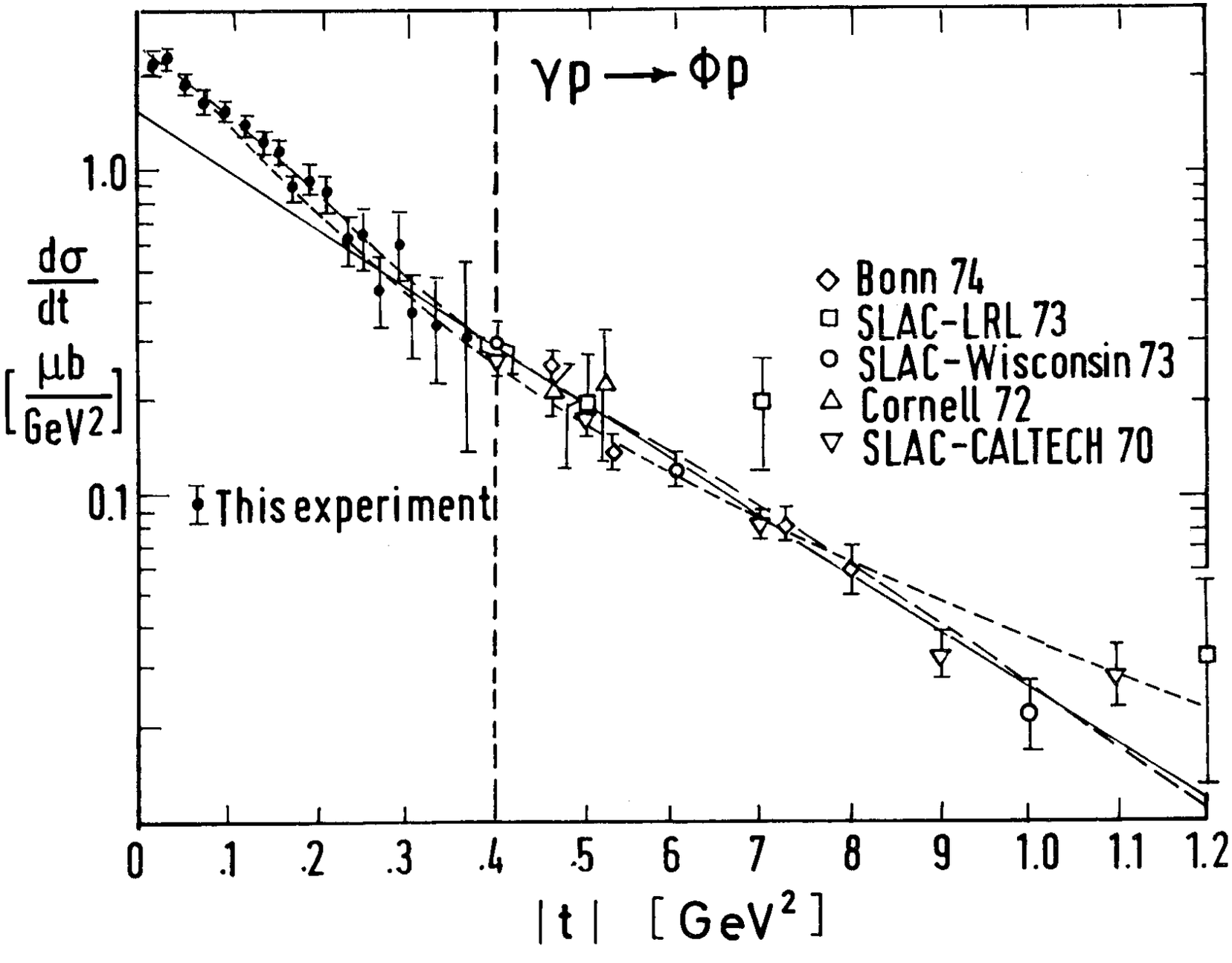
γp → Φp
1.0
0.1
dσ/dt
[μb/GeV²]
This experiment
Bonn 74
SLAC-LRL 73
SLAC-Wisconsin 73
Cornell 72
SLAC-CALTECH 70
0
.1
.2
.3
.4
.5
6
7
8
9
1.0
1.1
1.2
|t| [GeV²]

FIG.19

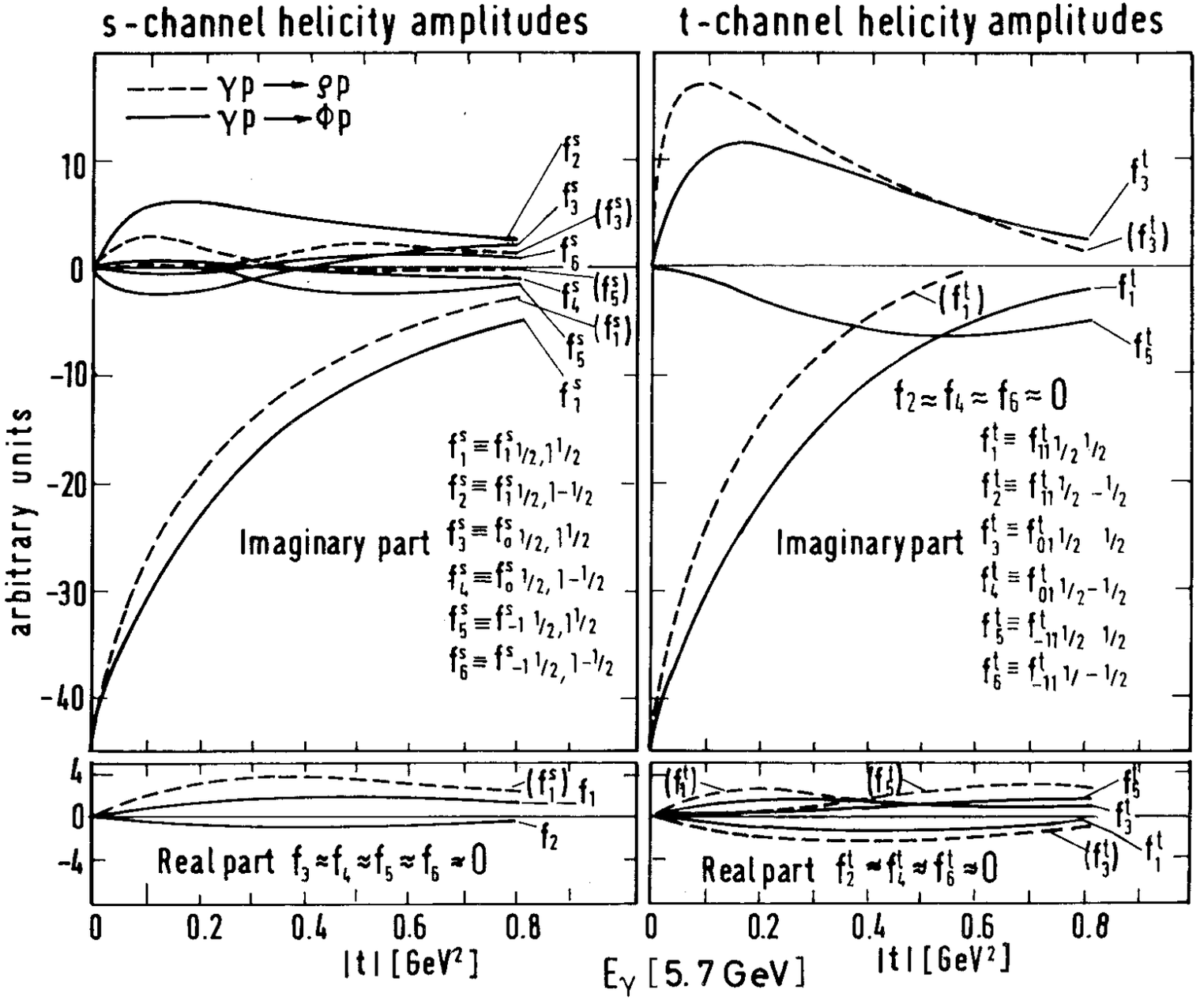
s-channel helicity amplitudes
t-channel helicity amplitudes
γp → ρp
γp → Φp
arbitrary units
Imaginary part
Real part
$f_1^s \equiv f_{1\,1/2,1\,1/2}^s$
$f_2^s \equiv f_{1\,1/2,1-1/2}^s$
$f_3^s \equiv f_{0\,1/2,1\,1/2}^s$
$f_4^s \equiv f_{0\,1/2,1-1/2}^s$
$f_5^s \equiv f_{-1\,1/2,1\,1/2}^s$
$f_6^s \equiv f_{-1\,1/2,1-1/2}^s$
$f_2 \approx f_4 \approx f_6 \approx 0$
$f_1^t \equiv f_{11\,1/2\,1/2}^t$
$f_2^t \equiv f_{11\,1/2\,-1/2}^t$
$f_3^t \equiv f_{01\,1/2\,1/2}^t$
$f_4^t \equiv f_{01\,1/2-1/2}^t$
$f_5^t \equiv f_{-11\,1/2\,1/2}^t$
$f_6^t \equiv f_{-11\,1/-1/2}^t$
$f_3 \approx f_4 \approx f_5 \approx f_6 \approx 0$
$f_2^t \approx f_4^t \approx f_6^t \approx 0$
|t| [GeV²]
E_γ [5.7 GeV]

FIG.20

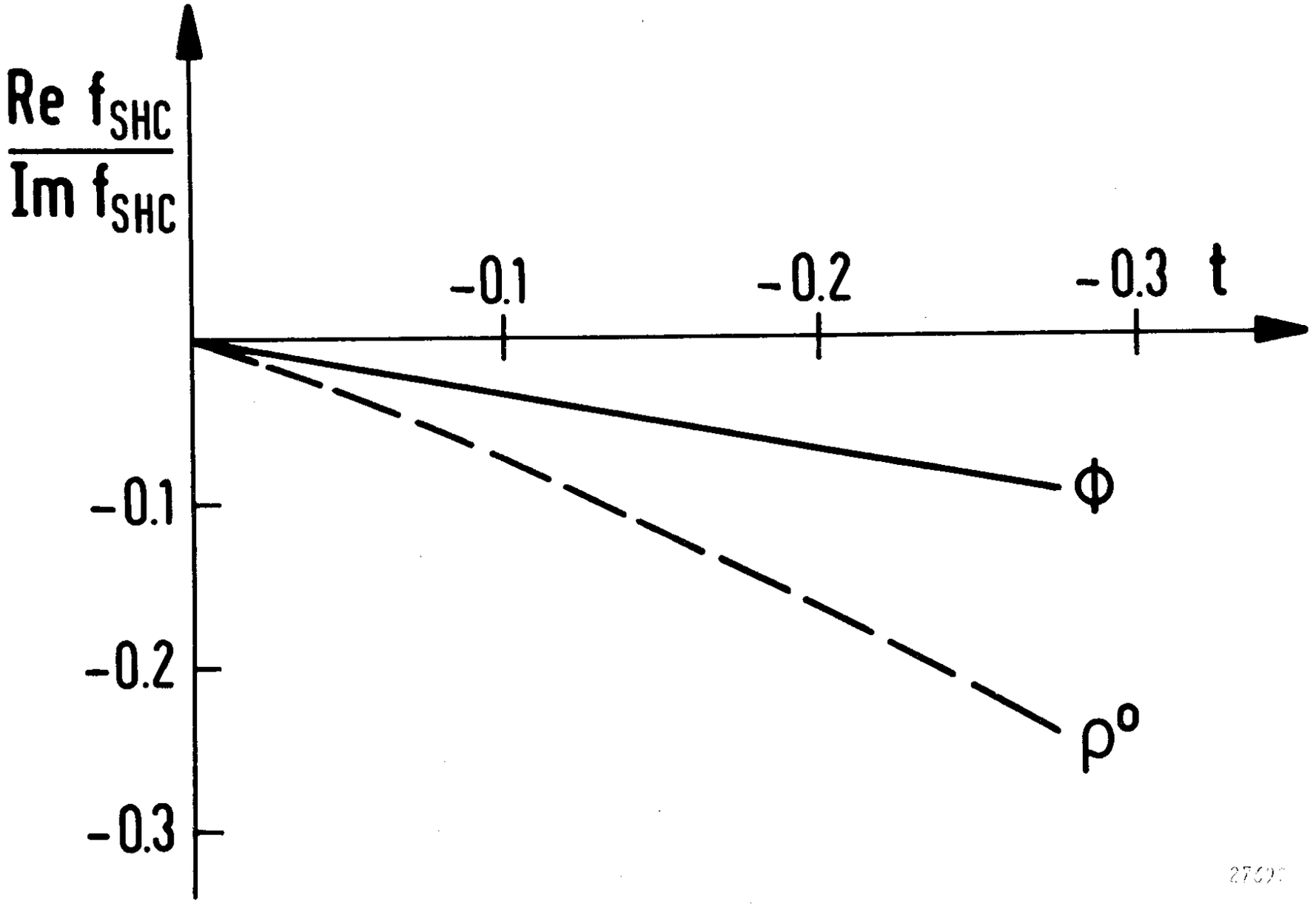

FIG.21

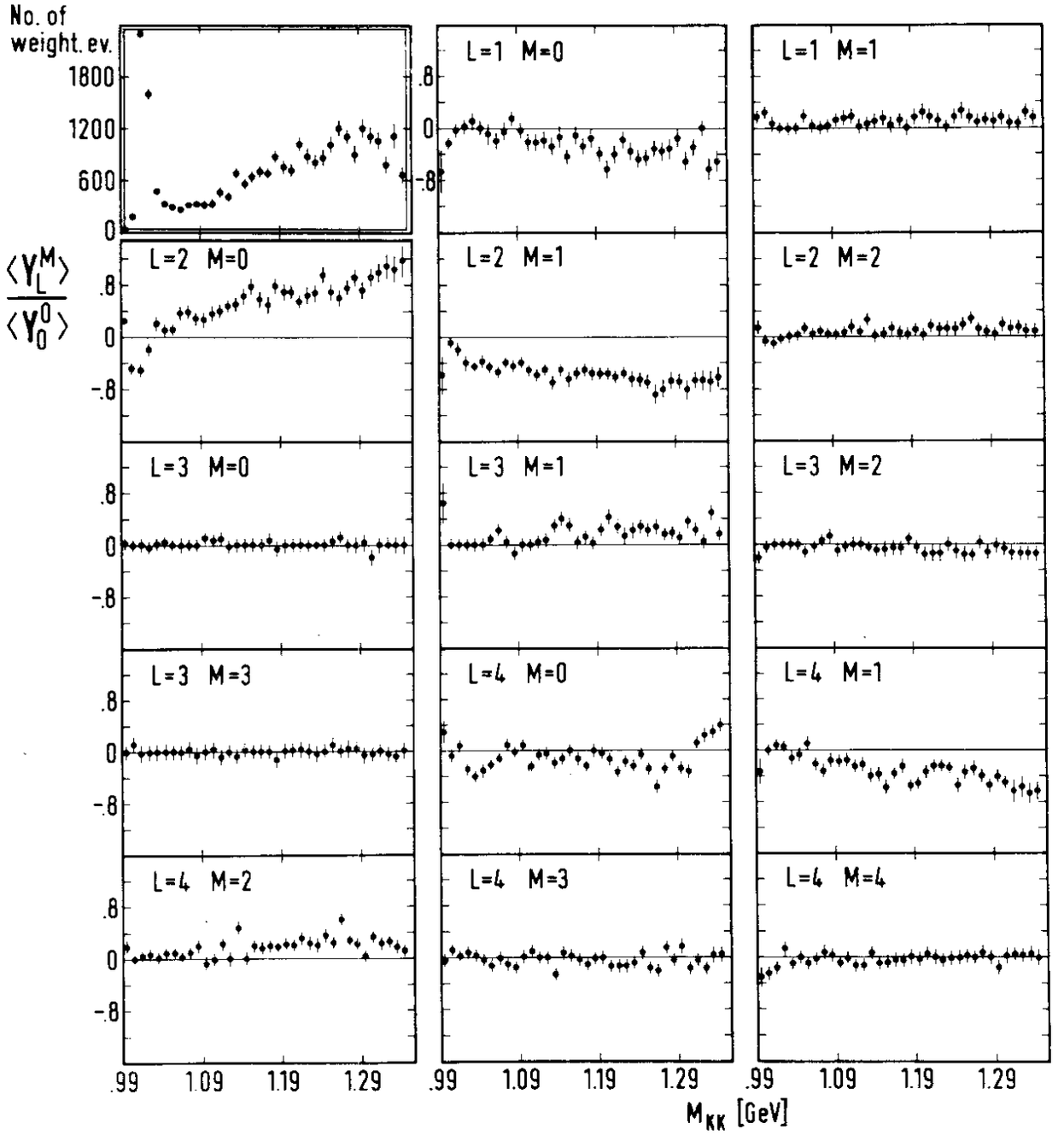
No. of weight. ev.
1800
1200
600
0
$\frac{\langle Y_L^M \rangle}{\langle Y_0^0 \rangle}$
L=1 M=0
L=1 M=1
L=2 M=0
L=2 M=1
L=2 M=2
L=3 M=0
L=3 M=1
L=3 M=2
L=3 M=3
L=4 M=0
L=4 M=1
L=4 M=2
L=4 M=3
L=4 M=4
.8
0
-.8
.99
1.09
1.19
1.29
M_{KK} [GeV]

FIG.22

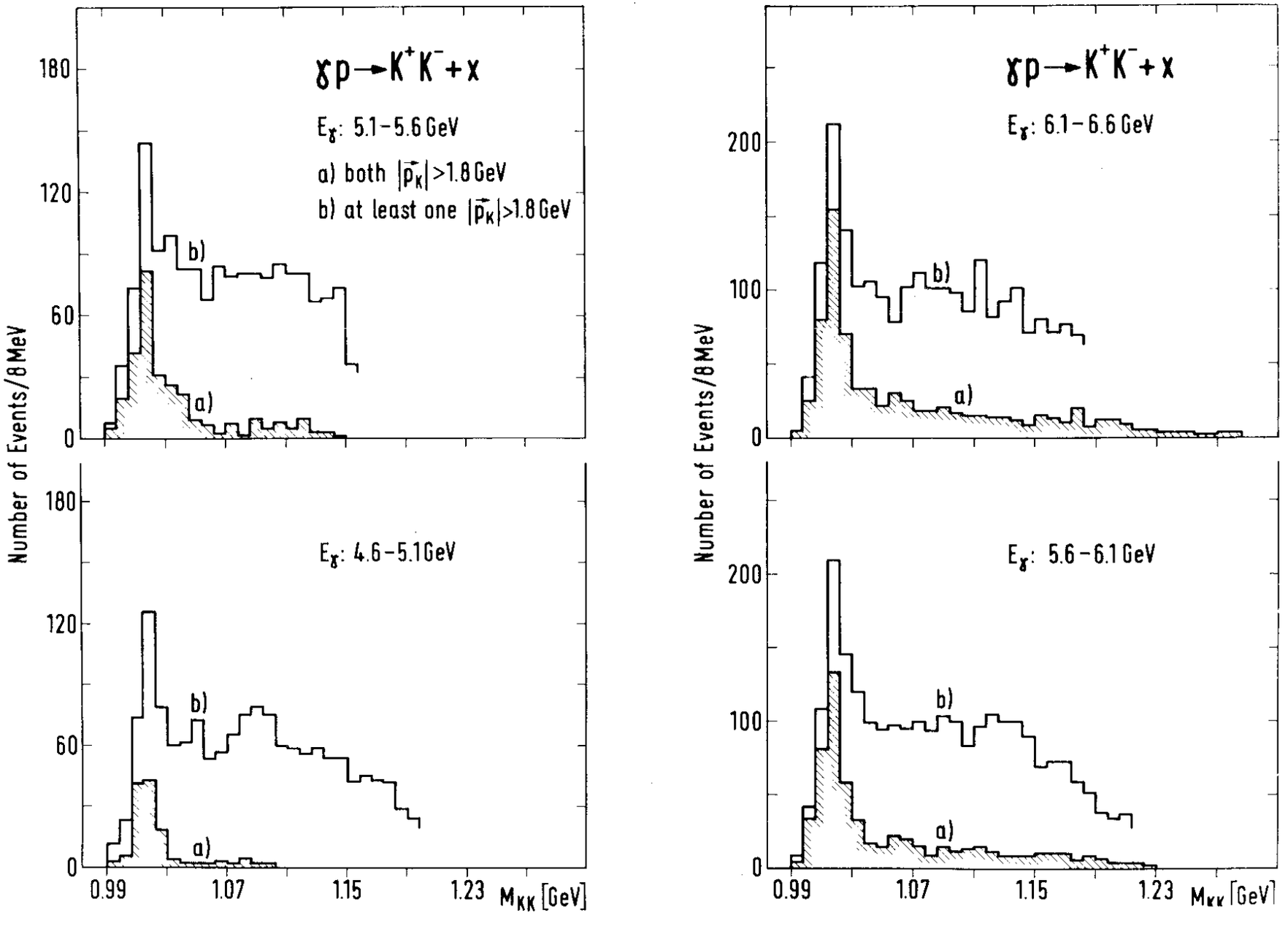
γp→K⁺K⁻+x
Eγ: 5.1–5.6 GeV
a) both |p⃗K|>1.8 GeV
b) at least one |p⃗K|>1.8 GeV
Eγ: 4.6–5.1 GeV
Eγ: 6.1–6.6 GeV
Eγ: 5.6–6.1 GeV
Number of Events/8 MeV
MKK [GeV]
0.99
1.07
1.15
1.23
0
60
120
180
100
200
a)
b)

FIG.23

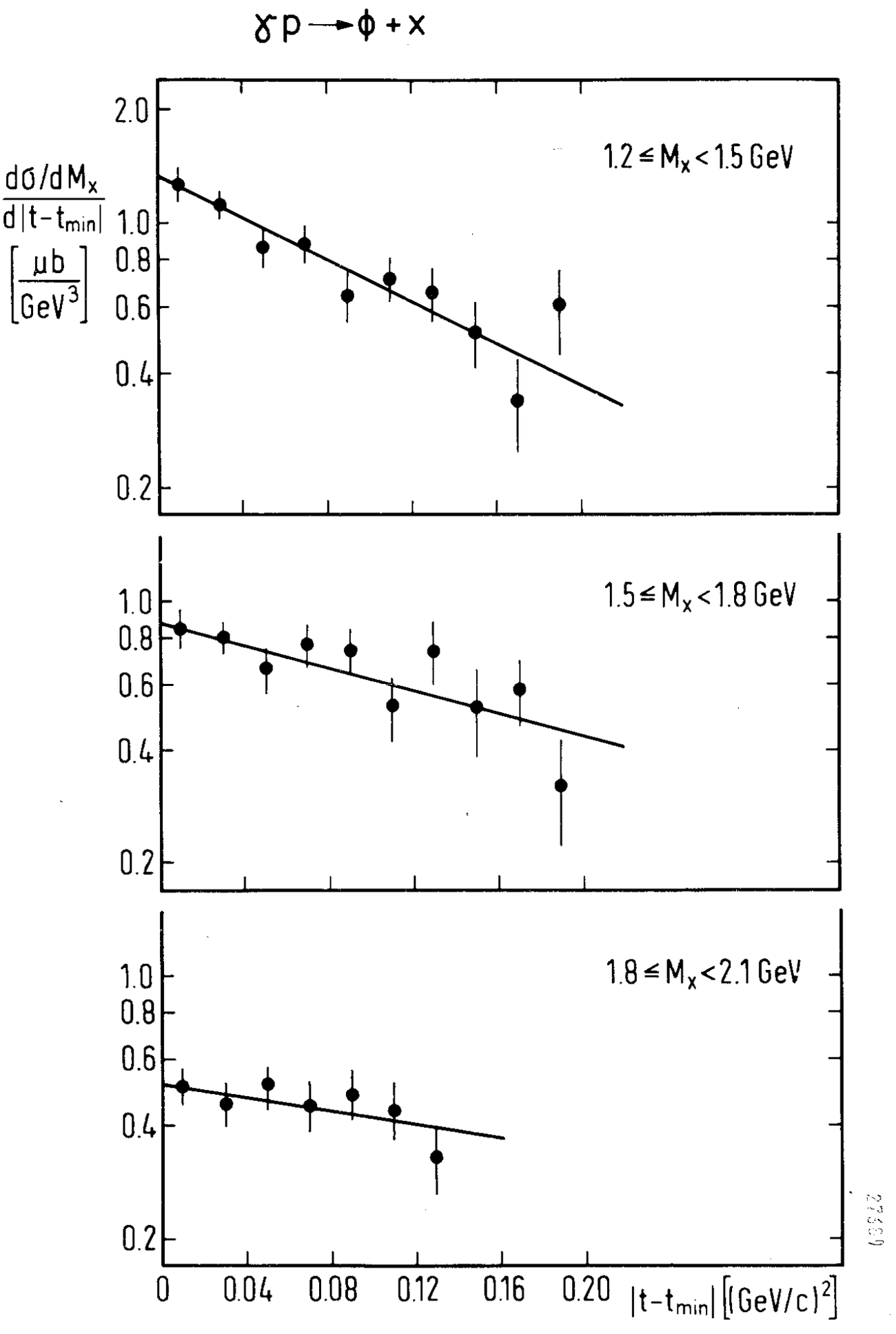
γp → φ + X
dσ/dM_x / d|t−t_min| [μb/GeV³]
1.2 ≤ M_x < 1.5 GeV
1.5 ≤ M_x < 1.8 GeV
1.8 ≤ M_x < 2.1 GeV
2.0
1.0
0.8
0.6
0.4
0.2
0
0.04
0.08
0.12
0.16
0.20
|t−t_min| [(GeV/c)²]

FIG.24

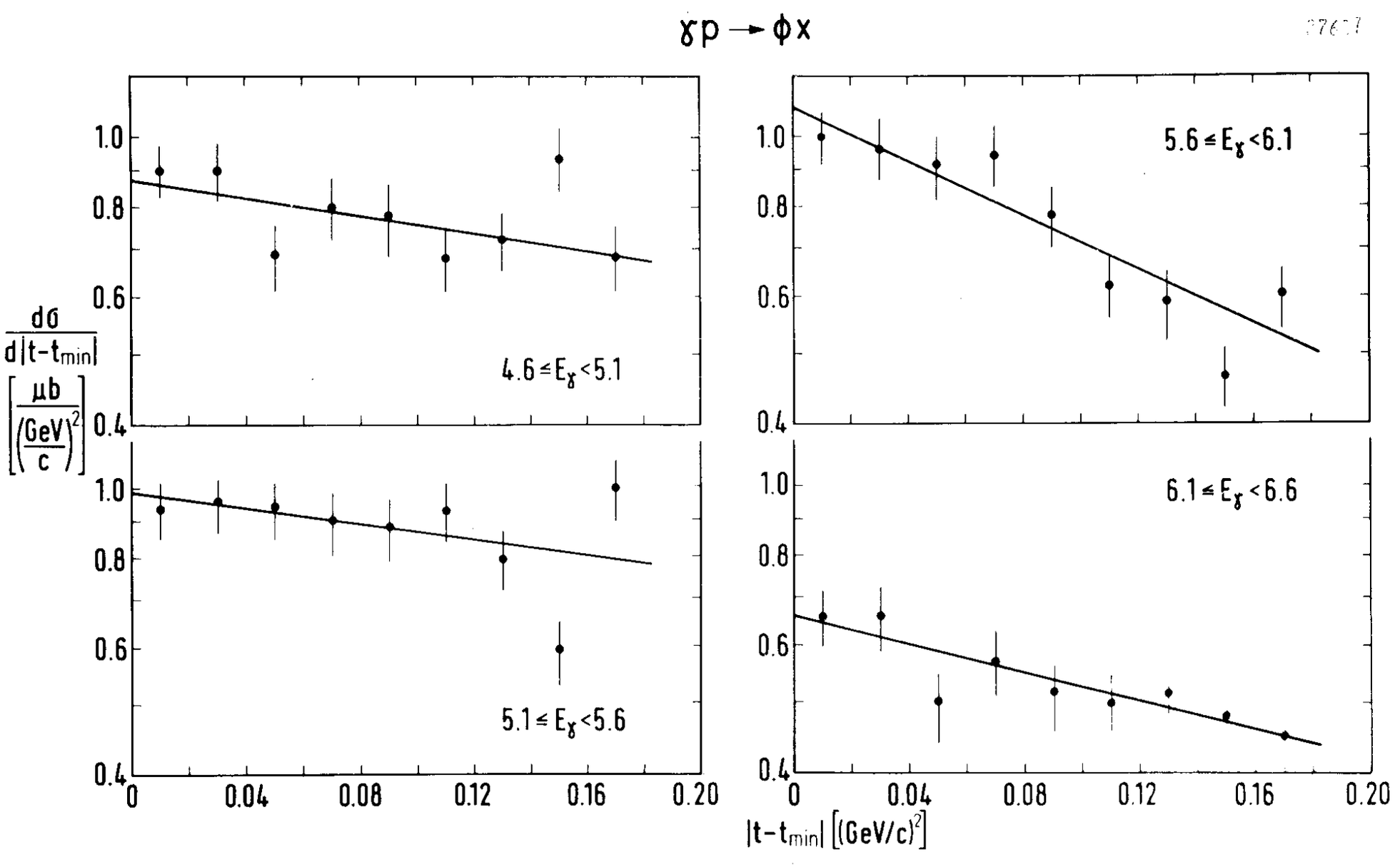
γp → φx
dσ / d|t-t_min| [μb / (GeV/c)²]
4.6 ≤ E_γ < 5.1
5.1 ≤ E_γ < 5.6
5.6 ≤ E_γ < 6.1
6.1 ≤ E_γ < 6.6
|t-t_min| [(GeV/c)²]
0
0.04
0.08
0.12
0.16
0.20
0.4
0.6
0.8
1.0

FIG.25

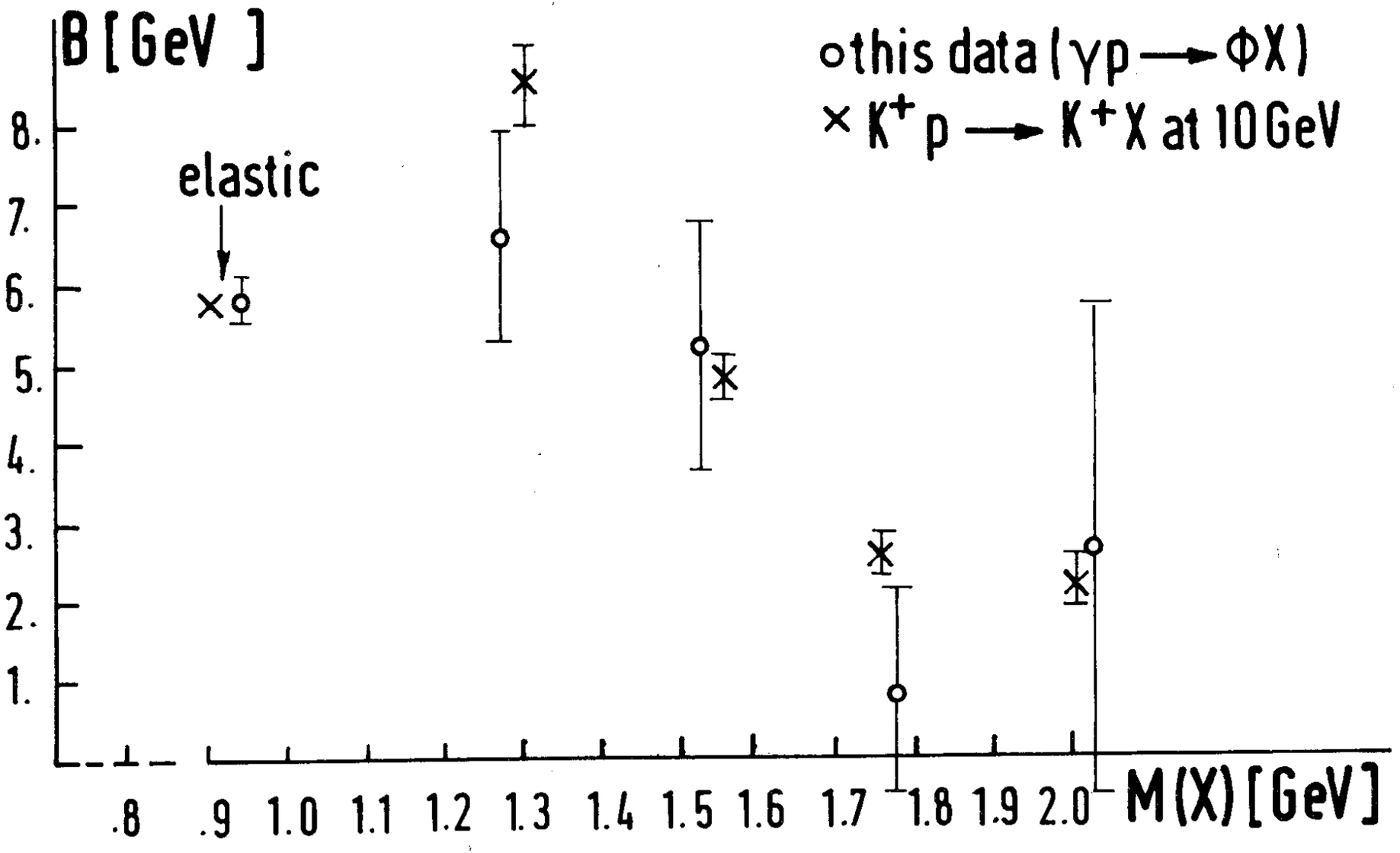
B [GeV]
o this data (γp → ΦX)
× K⁺p → K⁺X at 10 GeV
elastic
8.
7.
6.
5.
4.
3.
2.
1.
.8
.9
1.0
1.1
1.2
1.3
1.4
1.5
1.6
1.7
1.8
1.9
2.0
M(X) [GeV]

FIG.26

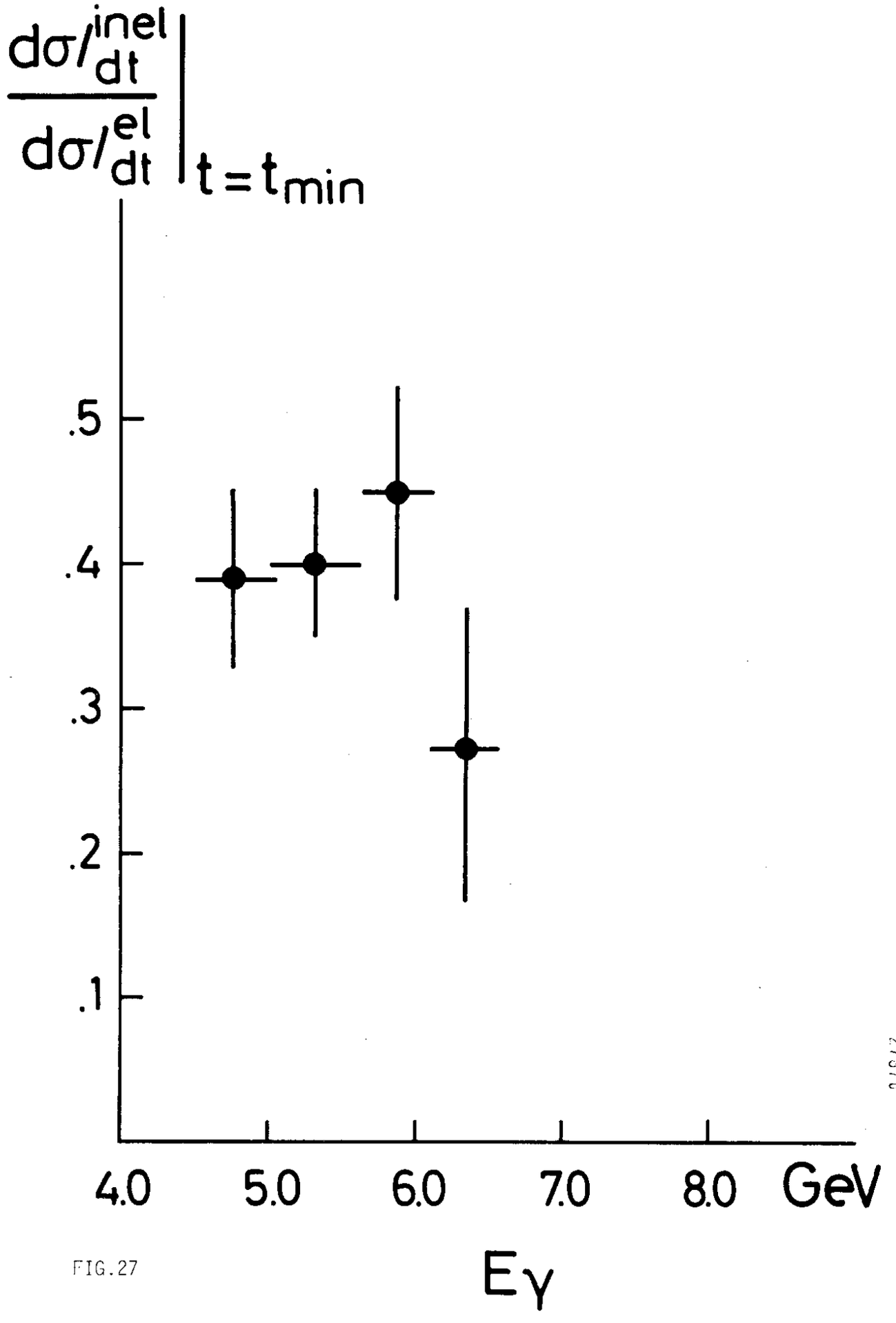
$\left.\frac{d\sigma/dt^{inel}}{d\sigma/dt^{el}}\right|_{t=t_{min}}$
.5
.4
.3
.2
.1
4.0
5.0
6.0
7.0
8.0
GeV
E_γ
27576

FIG.27